AKARI/IRC near-infrared asteroid spectroscopic survey: AcuA-spec

Usui, Fumihiko
Hasegawa, Sunao
Ootsubo, Takafumi
Onaka, Takashi

(Citation)
Publications of the Astronomical Society of Japan,71(1):1-1

(Issue Date)
2019-01

(Resource Type)
journal article

(Version)
Version of Record

(URL)
https://hdl.handle.net/20.500.14094/90005812

Publ. Astron. Soc. Japan (2019) 71 (1), 1 (1–41)
doi: 10.1093/pasj/psy125
Advance Access Publication Date: 2018 December 17

AKARI/IRC near-infrared asteroid spectroscopic survey: AcuA-spec

Fumihiko Usui,[1,*] Sunao Hasegawa,[2] Takafumi Ootsubo,[2] and Takashi Onaka[3]

[1]Center for Planetary Science, Graduate School of Science, Kobe University, 7-1-48 Minatojima-Minamimachi, Chuo-Ku, Kobe, Hyogo 650-0047, Japan
[2]Institute of Space and Astronautical Science, Japan Aerospace Exploration Agency, 3-1-1 Yoshinodai, Chuo-ku, Sagamihara, Kanagawa 252-5210, Japan
[3]Department of Astronomy, Graduate School of Science, The University of Tokyo, 7-3-1 Hongo, Bunkyo-ku, Tokyo 113-0033, Japan

*E-mail: usui@cps-jp.org

Received 2018 August 2; Accepted 2018 October 9

Abstract

Knowledge of water in the solar system is important for the understanding of a wide range of evolutionary processes and the thermal history of the solar system. To explore the existence of water in the solar system, it is indispensable to investigate hydrated minerals and/or water ice on asteroids. These water-related materials show absorption features in the 3 μm band (wavelengths from 2.7 to 3.1 μm). We conducted a spectroscopic survey of asteroids in the 3 μm band using the Infrared Camera (IRC) on board the Japanese infrared satellite AKARI. In the warm mission period of AKARI, 147 pointed observations were performed for 66 asteroids in the grism mode for wavelengths from 2.5 to 5 μm. According to these observations, most C-complex asteroids have clear absorption features (>10% with respect to the continuum) related to hydrated minerals at a peak wavelength of approximately 2.75 μm, while S-complex asteroids have no significant features in this wavelength range. The present data are released to the public as the Asteroid Catalog using AKARI Spectroscopic Observations (AcuA-spec).

Key words: infrared: planetary systems — minor planets, asteroids: general — space vehicles — techniques: spectroscopic

1 Introduction

Water is found in various forms in our solar system and is one of the most important ingredients in the origin of life. It also has vital implications for the exploration of extrasolar planets and provides evidence for the evolution of the solar system, especially its thermal history. Silicate minerals account for a large fraction of solid materials in the solar system and water exists as ice in small solar system bodies beyond Jupiter. Hydrated minerals (any mineral that contains H_2O or OH) are formed in environments where anhydrous rock and liquid water exist together with a certain pressure and temperature, resulting from aqueous alteration (e.g., Brearley 2006 and references cited therein). Because hydrated minerals are stable even above the sublimation temperature of water ice, they become an important tracer of water present in the history of the solar system, unless they were reset by a temperature change after formation. The study of hydrated minerals is therefore important

for understanding the origin of Earth's water and unravelling the earliest thermal processes in the solar system. Most asteroids have not experienced sufficient thermal evolution to differentiate into layered structures like terrestrial planets since their formation; thus, asteroids are considered to record the initial conditions of our solar nebula of 4.6 Ga ago. To explore the existence of water in the present solar system, it is necessary to investigate the presence of hydrated minerals and water ice on various types of asteroids.

Meteorites collected on the Earth have typically fallen from asteroids (e.g., Morbidelli & Gladman 1998) and bring useful information for asteroid research. However, it is difficult to measure the water content correctly because meteorites have been contaminated by atmospheric water (e.g., Beck et al. 2010; Takir et al. 2015a; Mogi et al. 2017). Observations with astronomical telescopes are needed to investigate asteroids without terrestrial alteration. Hydrated minerals and water ice exhibit diagnostic absorption features in the so-called 3 μm band (approximately 2.5–3.5 μm wavelength range; Rivkin et al. 2002). Features at $\sim$2.7 μm are attributed to hydrated minerals and those at $\sim$3.05 μm to water ice. Other materials also display spectral features at these wavelengths, such as ammonium-bearing phyllosilicate (King et al. 1992), mineral brucite (magnesium hydroxide; Beck et al. 2011), and absorbed water molecules in regolith particles (e.g., in lunar rocks or soils; Clark 2009). Many spectroscopic surveys have been conducted in the 3 μm band using ground-based observatories. Takir and Emery (2012) observed 28 outer main-belt asteroids with the NASA Infrared Telescope Facility (IRTF) on the summit of Mauna Kea, Hawaii, and classified them into four spectral groups based on the absorption shapes: sharp, rounded, Ceres-like, and Europa-like, and discussed the distribution and abundance of hydrated minerals in the outer main-belt region. However, space-borne telescopes can perform more accurate observations for the identification of mineral species, because the spectrum observed with a ground-based telescope (2.5–2.85 μm) is severely affected by telluric absorption (e.g., Rivkin et al. 2002).

AKARI (Murakami et al. 2007), launched in 2006, is a Japanese satellite mission fully dedicated to a wide range of infrared astronomy, including galaxy evolution, stellar formation and evolution, interstellar media, and solar system objects. As part of our research, we conducted two types of asteroid surveys with AKARI. One is a mid-infrared asteroid survey. Using the mid-infrared part of all-sky survey data obtained with the Infrared Camera (IRC; Onaka et al. 2007; Ishihara et al. 2010) on board AKARI, we constructed a size and albedo catalog of 5120 asteroids (Usui et al. 2011), which is summarized in the "Asteroid Catalog using AKARI" (AcuA).[1] This is an unbiased asteroid catalog at two mid-infrared bands (9 μm and 18 μm), which fully covers objects with a diameter of >40 km in the main-belt region (Usui et al. 2014). It was conducted using observations made during the cryogenic phase (Phase 1 and 2). The other survey is a near-infrared spectroscopic survey, which is described in this paper. Low-resolution spectroscopic observations were performed using the near-infrared channel (2.5–5 μm) of the IRC, which provides valuable data thanks to its high sensitivity and unique wavelength coverage (Ohyama et al. 2007). Note that the Infrared Space Observatory (ISO; Kessler et al. 1996) has a spectroscopic sensitivity to detect only the largest objects in the main-belt region (Dotto et al. 1999; Rivkin 1997) and that the Infrared Spectrograph (IRS) of the Spitzer Space Telescope (Werner et al. 2004) only covers wavelengths longer than 5 μm.

In this study, we report a spectroscopic survey of asteroids using the IRC on board AKARI. During the warm mission period of AKARI (Phase 3; Onaka et al. 2012), 147 pointed observations were performed for 66 asteroids in the grism mode at wavelengths from 2.5 to 5 μm. The observed objects comprise C-complex (×23), S-complex (×17), X-complex (×22), D-complex (×3), and V-type (×1) asteroids, all of which are in the main-belt region and have diameters of 40 km or larger.

This paper is organized as follows: section 2 describes the observations of asteroids made with AKARI and the data reduction process used to derive reflectance spectra; section 3 presents the characteristics of the obtained spectra; and the results are discussed in section 4.

2 Observations and data reduction

2.1 NIR grism spectroscopic observations with the AKARI/IRC

AKARI was launched on 2006 February 21 UT, and its liquid helium cryogen boiled off on 2007 August 26 UT, 550 days after the launch (Murakami et al. 2007). This cryogenic phase is referred to as Phase 1 and 2. In the post-helium phase (Phase 3), the telescope and its scientific instruments were maintained at approximately 40 K by the mechanical cooler and only near-infrared observations were carried out until 2010 February. The main purpose of AKARI was to perform all-sky surveys during Phase 1 and 2 by continuous scanning of the sky at a constant scan speed; i.e., in the survey observation mode. AKARI also

[1] This catalog, as well as the infrared flux data of individual asteroids (Alí-Lagoa et al. 2018), is open to the public at the following URLs: ⟨http://darts.isas.jaxa.jp/astro/akari/catalogue/AcuA.html⟩ and ⟨http://www.ir.isas.jaxa.jp/AKARI/Archive/Catalogues/Asteroid_Flux_V1/⟩.

has the capability to make a pointed observation, which is occasionally inserted into the continuous survey observation (the observational strategy of AKARI is discussed in Matsuhara et al. 2005). In Phase 3, only pointed observations with IRC were available, in which the same attitude control mode was employed as during Phase 1 and 2 operations. This pointed observation mode is employed for deep imaging or spectroscopy.

Our targets were 66 objects selected from main-belt asteroids, the Cybeles, the Hildas, and one near-Earth object, 4015 Wilson-Harringtion, according to the visibility from AKARI. Most of these observations were performed as part of the AKARI Mission Program entitled "Origin and Evolution of Solar System Objects" (SOSOS), while four observations were executed within the framework of the AKARI director's time program (DT): two observations were made for 6 Hebe and the other two for 128 Nemesis. The physical properties and taxonomic classification of our targets are summarized in tables 1 and 2. All objects have entries of the size and albedo (Usui et al. 2011; Mainzer et al. 2011), rotational period (Warner et al. 2009),[2] and taxonomic information from visible to near-infrared wavelengths (from 0.4–2.5 μm; hereafter vis-NIR) compiled by Hasegawa et al. (2017). The distribution of the orbital elements and the size and albedo diagrams of our targets are shown in figures 1 and 2, respectively.

Observations were conducted 147 times from 2008 May to 2010 February. Observation logs are given in table 3. Typically, two or three pointed observations were performed for each target, whereas three targets (8 Flora, 69 Hesperia, and 4015 Wilson-Harrington) were observed only once. Most objects were observed within ~100 min intervals, which matched the orbital period of the satellite. Exceptions are 216 Kleopatra and 704 Interamnia, both of which were observed at intervals of more than 14 months because of the scheduling constraint, but not for any scientific reason. The direction of AKARI observations was severely limited to within $90^\circ \pm 0.^\circ 7$ of the solar elongation angle due to the design of the orbit and attitude control system to avoid radiation from the Earth and the Sun. Within this geometric constraint, our targets in the main-belt region were located between phase angles of 15° and 32°. We made observations with the AKARI Astronomical Observation Template (AOT) of spectroscopy dedicated to Phase 3 (IRCZ4; see the IRC Data User Manual),[3] which is equivalent to IRC04 in Phase 1 and 2 (Onaka et al. 2007; Ohyama et al. 2007). The grism mode covered a wavelength range of 2.5–5 μm with a spectral resolution of $R \sim 100$. Within a single AOT operation lasting approximately 10 min, eight or nine spectroscopic images were taken with the grism, as well as a photometric image (called a reference image) through a broad-band filter in the wavelength range of 2.7–3.8 μm centered at 3.2 μm (the N3 band). The effective exposure time for each frame was 44.41 s (see the IRC Data User Manual). Total exposure time of one pointed observation is 310–400 s depending on the attitude stability of the satellite; thus our observations provided a flux-limited sample. The targets were put on the $1' \times 1'$ aperture mask (the "Np" window; Onaka et al. 2007, also see figure 3) to minimize contamination from nearby objects (e.g., Ootsubo et al. 2012). AKARI was also equipped with narrow slits ("Nh" of width of 3″ and "Ns" of width of 5″); however, these modes were designed for diffuse sources. The absolute accuracy of the telescope pointing of the satellite is a few arcseconds; thus, we used the Np window instead of Nh or Ns slits for point sources. For the Np observations, it was not necessary to consider slit loss because of the large width of this mask. Note that the full width at the half-maximum of the point spread function (PSF) in the N3 band is 3.2 pixels or 4.″67 (Onaka et al. 2008, 2010; see also the IRC Data User Manual).

2.2 Data reduction

Figure 3 shows an example of data reduction for C-type asteroid 511 Davida (Obs ID:1520065-001).

2.2.1 Extraction of one-dimensional spectra

The raw data were reduced using the IDL-based software package in the IRC Spectroscopy Toolkit for Phase 3 data, version 20170225RC (Ohyama et al. 2007; Usui et al. 2018; see also the IRC Data User Manual). Standard array image processing, such as dark subtraction, cosmic-ray removal, linearity correction, and various image anomaly corrections (bad-pixel masking, correction of tilt of the spectrum, and the first-order sky subtraction), were first performed for each exposure frame with the toolkit. Then, multiple-exposure frames were added, taking into account the relative image shift due to the satellite attitude drift among the frames. Because AKARI does not have a tracking mode for moving objects, the resulting two-dimensional spectra with the standard toolkit was blurred due to motion of the object. Note that the velocities of apparent motion of the targets were typically less than 7.″5/10 min (or ~5 pixel/10 min); thus, the targets were located within the field of view of the Np window during the observations (with the exception of 4015 Wilson-Harrington, which was 30″/10 min). The movements of the target asteroid during the observation of each frame were calculated to add to the relative image shift, and multiple-exposure frames were shift-and-added

[2] Updated 2018 March 7 ⟨http://www.MinorPlanet.info/lightcurvedatabase.html#top⟩.

[3] ⟨http://www.ir.isas.jaxa.jp/AKARI/Observation/support/IRC/⟩.

Table 1. Physical properties of our targets.

Object	a^* [au]	i^* [°]	e^*	Region	$H^\dagger$	$G^\dagger$	$d^\dagger$ [km]	$p_v{}^\dagger$	$P_{rot}{}^\ddagger$ [hr]
1 Ceres	2.767	10.594	0.076	Middle MBA	3.34	0.12	973.9	0.087	9.07
2 Pallas	2.772	34.837	0.230	Middle MBA	4.13	0.11	512.6	0.150	7.81
4 Vesta	2.362	7.141	0.089	Inner MBA	3.20	0.32	521.7	0.342	5.34
5 Astraea	2.574	5.368	0.191	Middle MBA	6.85	0.15	110.8	0.263	16.81
6 Hebe	2.425	14.737	0.203	Inner MBA	5.71	0.24	197.2	0.238	7.27
7 Iris	2.385	5.524	0.231	Inner MBA	5.51	0.15	254.2	0.179	7.14
8 Flora	2.201	5.887	0.157	Inner MBA	6.49	0.28	138.3	0.235	12.87
9 Metis	2.386	5.577	0.123	Inner MBA	6.28	0.17	166.5	0.213	5.08
10 Hygiea	3.141	3.832	0.113	Outer MBA	5.43	0.15	428.5	0.066	27.63
13 Egeria	2.578	16.539	0.084	Middle MBA	6.74	0.15	203.4	0.086	7.04
16 Psyche	2.927	3.095	0.134	Outer MBA	5.90	0.20	207.2	0.181	4.20
21 Lutetia	2.436	3.064	0.164	Inner MBA	7.35	0.11	108.4	0.181	8.17
22 Kalliope	2.912	13.718	0.099	Outer MBA	6.45	0.21	139.8	0.239	4.15
24 Themis	3.137	0.752	0.125	Outer MBA	7.08	0.19	176.8	0.084	8.37
33 Polyhymnia	2.876	1.854	0.332	Outer MBA	8.55	0.33	54.0	0.232	18.61
40 Harmonia	2.267	4.257	0.047	Inner MBA	7.0	0.15	110.3	0.233	8.91
42 Isis	2.442	8.514	0.223	Inner MBA	7.53	0.15	104.5	0.158	13.59
44 Nysa	2.423	3.707	0.148	Inner MBA	7.03	0.46	75.7	0.479	6.42
46 Hestia	2.525	2.350	0.172	Middle MBA	8.36	0.06	120.6	0.055	21.04
49 Pales	3.103	3.175	0.224	Outer MBA	7.8	0.15	148.0	0.061	20.70
50 Virginia	2.649	2.838	0.286	Middle MBA	9.24	0.15	84.4	0.050	14.31
51 Nemausa	2.366	9.980	0.067	Inner MBA	7.35	0.08	147.2	0.094	7.78
52 Europa	3.093	7.479	0.110	Outer MBA	6.31	0.18	350.4	0.043	5.63
55 Pandora	2.760	7.180	0.143	Middle MBA	7.7	0.15	63.3	0.337	4.80
56 Melete	2.596	8.080	0.238	Middle MBA	8.31	0.15	105.2	0.076	18.15
64 Angelina	2.682	1.310	0.126	Middle MBA	7.67	0.48	54.3	0.515	8.75
65 Cybele	3.427	3.563	0.112	Cybeles	6.62	0.01	300.5	0.044	6.08
69 Hesperia	2.976	8.593	0.170	Outer MBA	7.05	0.19	132.7	0.157	5.66
79 Eurynome	2.446	4.617	0.191	Inner MBA	7.96	0.25	74.8	0.209	5.98
81 Terpsichore	2.853	7.804	0.211	Outer MBA	8.48	0.15	123.0	0.048	10.94
87 Sylvia	3.482	10.877	0.093	Cybeles	6.94	0.15	262.7	0.043	5.18
89 Julia	2.551	16.127	0.185	Middle MBA	6.60	0.15	146.8	0.188	11.39
92 Undina	3.187	9.931	0.104	Outer MBA	6.61	0.15	120.9	0.275	15.94
94 Aurora	3.156	7.971	0.094	Outer MBA	7.57	0.15	179.2	0.053	7.22
106 Dione	3.180	4.597	0.165	Outer MBA	7.41	0.15	153.4	0.084	16.21
121 Hermione	3.448	7.598	0.133	Cybeles	7.31	0.15	194.1	0.058	5.55
127 Johanna	2.755	8.246	0.067	Middle MBA	8.5	0.15	114.2	0.065	12.80
128 Nemesis	2.750	6.245	0.127	Middle MBA	7.49	0.15	177.9	0.059	77.81
129 Antigone	2.869	12.264	0.212	Outer MBA	7.07	0.33	119.5	0.185	4.96
135 Hertha	2.428	2.305	0.207	Inner MBA	8.23	0.15	72.8	0.171	8.40
140 Siwa	2.734	3.185	0.214	Middle MBA	8.34	0.15	110.6	0.067	34.45
145 Adeona	2.673	12.635	0.144	Middle MBA	8.13	0.15	141.4	0.050	15.07
148 Gallia	2.771	25.291	0.187	Middle MBA	7.63	0.15	80.9	0.240	20.66
153 Hilda	3.980	7.827	0.140	Hildas	7.48	0.15	163.5	0.068	5.96
161 Athor	2.379	9.060	0.138	Inner MBA	9.15	0.13	40.8	0.233	7.28
173 Ino	2.743	14.196	0.209	Middle MBA	7.66	0.01	160.6	0.059	6.15
185 Eunike	2.737	23.238	0.129	Middle MBA	7.62	0.15	167.7	0.057	21.80
216 Kleopatra	2.794	13.113	0.251	Middle MBA	7.30	0.29	121.5	0.149	5.38
246 Asporina	2.695	15.620	0.110	Middle MBA	8.62	0.15	59.9	0.177	16.22
250 Bettina	3.144	12.820	0.135	Outer MBA	7.58	0.15	109.4	0.142	5.05
308 Polyxo	2.749	4.362	0.040	Middle MBA	8.17	0.21	135.2	0.052	12.03
336 Lacadiera	2.252	5.654	0.095	Inner MBA	9.76	0.15	69.2	0.047	13.70
349 Dembowska	2.923	8.246	0.091	Outer MBA	5.93	0.37	164.7	0.277	4.70

Table 1. (Continued)

Object	a^* [au]	i^* [°]	e^*	Region	$H^\dagger$	$G^\dagger$	$d^\dagger$ [km]	$p_v{}^\dagger$	$P_{rot}{}^\ddagger$ [hr]
354 Eleonora	2.799	18.398	0.114	Middle MBA	6.44	0.37	149.6	0.211	4.28
361 Bononia	3.957	12.626	0.213	Hildas	8.22	0.15	151.8	0.040	13.84
371 Bohemia	2.726	7.397	0.065	Middle MBA	8.72	0.15	45.7	0.277	10.74
387 Aquitania	2.740	18.113	0.235	Middle MBA	7.41	0.15	105.1	0.174	24.14
419 Aurelia	2.597	3.926	0.251	Middle MBA	8.42	0.15	122.4	0.051	16.78
423 Diotima	3.067	11.244	0.036	Outer MBA	7.24	0.15	226.9	0.049	4.78
451 Patientia	3.061	15.239	0.075	Outer MBA	6.65	0.19	234.9	0.071	9.73
476 Hedwig	2.650	10.925	0.072	Middle MBA	8.55	0.15	111.1	0.055	27.33
511 Davida	3.164	15.938	0.188	Outer MBA	6.22	0.16	291.0	0.070	5.13
532 Herculina	2.773	16.314	0.176	Middle MBA	5.81	0.26	216.8	0.184	9.40
704 Interamnia	3.059	17.308	0.155	Outer MBA	5.94	-0.02	316.2	0.075	8.73
773 Irmintraud	2.858	16.667	0.079	Outer MBA	9.1	0.15	87.1	0.053	6.75
4015 Wilson-Harrington	2.627	2.798	0.631	NEA (Apollo)	15.99	0.15	3.8	0.046	3.57

*Orbital elements. Semimajor axis (a), inclination angle (i), and eccentricity (e) obtained from the Asteroid Orbital Elements Database of the Lowell Observatory, retrieved on 2018 May 29 ⟨ftp://ftp.lowell.edu/pub/elgb/astorb.html⟩.

†Absolute magnitude (H), slope parameter (G), diameter (d), and albedo (p_v) from Usui et al. (2011). Data of 4015 Wilson-Harrington is from Mainzer et al. (2011).

‡Rotational period. Warner, Harris, and Pravec (2009), updated on 2018 March 7 ⟨http://www.MinorPlanet.info/lightcurvedatabase.html⟩.

to extract a two-dimensional spectral image of the objects. This function was implemented in the toolkit for the data of solar system objects (details are given in Ootsubo et al. 2012). Using the combination of shift-and-add with the movement of the asteroid and the 3σ clipping methods, the effects of hot pixels were reduced in the stacked images, although the number of hot pixels in Phase 3 increased compared with Phase 1 and 2. The fluctuation of the background signals causes a random noise of the flux uncertainties of the target spectra. With the standard toolkit, the sky background was estimated from the adjacent region of the target in the Np window and subtracted from the stacked images. In some cases, however, the background signals are not able to be estimated properly from the adjacent region because of contamination of neighboring stars in the Np window. In this study, wavelength-dependent sky background was estimated from the diffuse sky spectrum of the Ns slit for the same pointed observation which was checked as contamination-free "blank" sky by visual inspection.

The absolute flux calibration (spectral response calibration) of the AKARI/IRC spectroscopy is based on the observation of active galactic nuclei (AGNs) and spectroscopic standard stars obtained with the same instrumental setup. The AGNs without significant emission or absorption features are used as calibrators of redder objects (contributed in longer wavelengths), and the standard stars whose spectra are already templated are used as bluer objects (contributed in shorter wavelengths). 13 featureless AGNs and six K- and A-type standard stars were selected as flux templates. The observations of these objects were performed within the framework of the DT program, separately from individual observations. Comparing the modeled templates of the objects with the observed flux count in analog-to-digital units (ADU), the spectral response was obtained as a function of wavelength. This spectral response was implemented in the toolkit. Details are given in Baba et al. (2016, 2019).

In general, the spectroscopic flat-fields are made by gathering a large number of blank sky spectroscopy images that are combined and normalized so that any faint object spectra are removed by clipping averaging techniques. For the AKARI observations, flat data were not taken in individual pointed observations because the observational time was severely limited due to the avoidance constraints of the satellite. As the natural background is faint in the near-infrared for small-aperture spectroscopy of the IRC (Np, Ns, and Nh), the quality of the flat data cannot be improved substantially even after stacking of multi-pointed observational data. Thus, the quality of the processed spectra is, unfortunately, limited by the quality of the flat data, not by the dark current or photon noise. If the spectra have low signal-to-noise (S/N) ratios, then applying a flat could degrade the data. Therefore, we skipped performing flat-fielding in the data reduction process (with an option called `/no_slit_flat` prepared to disable the flat correction in the toolkit: see the IRC Data User Manual).

It is reported that the sensitivity decreased by a maximum of approximately 10% during Phase 3 with the increase of the IRC detector temperature (Onaka et al. 2010). This can be approximated by a linear function of

Table 2. Taxonomy of our targets in the literature.

Object	Th*	B†	Th-L‡	B-L§	B-D‖	3 μm band shape#
1 Ceres	G	C	C	C	C	Ceres-like**
2 Pallas	B	B	—	—	B	—
4 Vesta	V	V	—	—	V	—
5 Astraea	S	S	—	—	S	—
6 Hebe	S	S	—	—	S	—
7 Iris	S	S	—	—	S	—
8 Flora	S	—	—	—	Sw	—
9 Metis	S	—	S	T	L	—
10 Hygiea	C	C	—	—	C	Ceres-like
13 Egeria	G	Ch	—	—	Ch	Sharp††
16 Psyche	M	X	—	—	Xk	—
21 Lutetia	M	Xk	X	X	Xc	—
22 Kalliope	M	X	—	—	X	—
24 Themis	C	B	Caa	C	C	Rounded
33 Polyhymnia	S	Sq	S	S	S	—
40 Harmonia	S	S	—	—	S	—
42 Isis	S	L	—	—	K	—
44 Nysa	E	Xc	—	—	Xn	—
46 Hestia	P	Xc	—	—	Xc	—
49 Pales	CG	Ch	—	—	Ch	—
50 Virginia	X	Ch	Caa	C	Ch	—
51 Nemausa	CU	Ch	—	—	Cgh	—
52 Europa	CF	C	—	—	C	Europa-like
55 Pandora	M	X	—	—	Xk	—
56 Melete	P	Xk	X	X	Xk	—
64 Angelina	E	Xe	—	—	Xe	—
65 Cybele	P	Xc	X	C	Xk	Rounded‡‡
69 Hesperia	M	X	—	—	Xk	—
79 Eurynome	S	S	—	—	S	—
81 Terpsichore	C	Cb	—	—	C	—
87 Sylvia	P	X	X	X	X	—
89 Julia	S	K	S	Ld	Sw	—
92 Undina	X	Xc	—	—	Xk	—
94 Aurora	CP	C	—	—	C	—
106 Dione	G	Cgh	Caa	Cgh	Cgh	—
121 Hermione	C	Ch	—	—	Ch	Sharp
127 Johanna	CX	Ch	Caa	Ch	Ch	—
128 Nemesis	C	C	—	—	C	—
129 Antigone	M	X	—	—	Xk	—
135 Hertha	M	Xk	—	—	Xk	—
140 Siwa	P	Xc	C	Cb	Xc	Featureless
145 Adeona	C	Ch	Caa	Ch	Ch	—
148 Gallia	GU	S	S	Sl	S	—
153 Hilda	P	X	—	—	X	Rounded
161 Athor	M	Xc	—	—	Xc	—
173 Ino	C	Xk	X	X	Xk	—
185 Eunike	C	C	—	—	C	—
216 Kleopatra	M	Xe	—	—	Xe	—
246 Asporina	A	A	A	L	A	—
250 Bettina	M	Xk	—	—	Xk	—
308 Polyxo	T	T	—	—	T	Sharp
336 Lacadiera	D	Xk	—	—	Xk	—
349 Dembowska	R	R	—	—	R	—
354 Eleonora	S	Sl	S	S	A	—

Table 2. (Continued)

Object	Th*	B†	Th-L‡	B-L§	B-D‖	3 μm band shape#
361 Bononia	DP	—	D	D	D	Rounded
371 Bohemia	QSV	S	—	—	S	—
387 Aquitania	S	L	—	—	L	—
419 Aurelia	F	—	C	Cb	C	—
423 Diotima	C	C	—	—	C	—
451 Patientia	CU	—	C	Cb	C	Europa-like
476 Hedwig	P	X	—	—	Xk	—
511 Davida	C	C	X	X	C	Sharp
532 Herculina	S	S	—	—	S	—
704 Interamnia	F	B	C	B	Cb	Sharp
773 Irmintraud	D	T	—	—	T	—
4015 Wilson-Harrington	CF	—	—	—	B	—

*Tholen taxonomy (Tholen 1984).
†Bus taxonomy (Bus & Binzel 2002).
‡Tholen taxonomy (Lazzaro et al. 2004).
§Bus taxonomy (Lazzaro et al. 2004).
‖Bus–DeMeo taxonomy summarized by Hasegawa et al. (2017). 4015 Wilson-Harrington is classified based on its available spectroscopic data (SMASS, Database of The MIT-UH-IRTF Joint Campaign for NEO Spectral Reconnaissance ⟨http://smass.mit.edu/⟩; Zellner et al. 1985; Ishiguro et al. 2011; Thomas et al. 2014).
#Takir and Emery (2012).
**Rivkin et al. (2006a).
††Takir, Emery, and McSween (2015a).
‡‡Licandro et al. (2011).

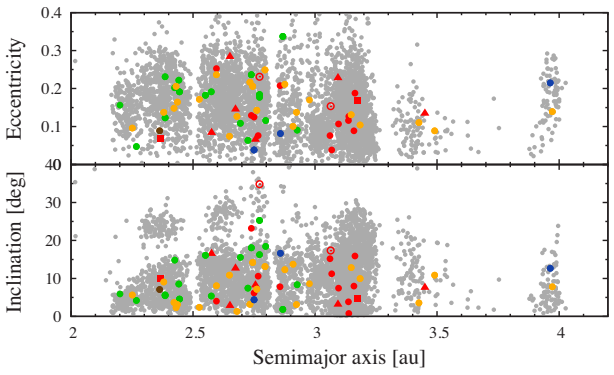

Fig. 1. Distribution of the orbital elements (semi-major axis, inclination, and eccentricity) of our target asteroids. Red, green, yellow, blue, and brown denote C-, S-, X-, D-complex, and V-type asteroids, respectively. C-complex asteroids are subdivided into rectangles, triangles, open circles, and filled circles, as Cgh-, Ch-, B or Cb, and other C-type, respectively. Gray dots are all asteroids taken from AcuA data (Usui et al. 2011). (Color online).

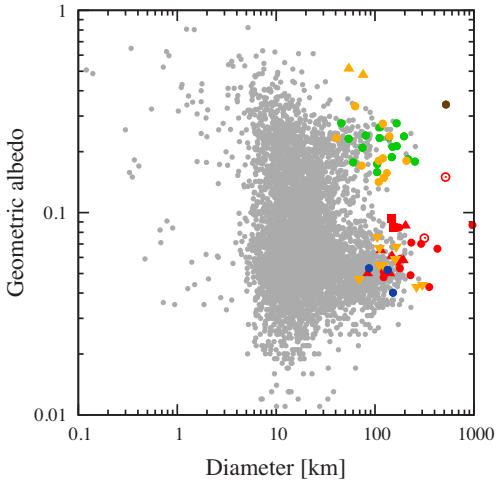

Fig. 2. Size and geometric albedo distribution of our targets. Colors and marks are the same as in figure 1. (Color online).

the detector temperature T (Baba et al. 2019) as

$$f(T) = 1 + a(T - T_0), \quad (1)$$

where $f(T)$ is the correction factor, $a = -0.0290\,\mathrm{K}^{-1}$ and $T_0 = 43.55\,\mathrm{K}$. For Obs ID:1521116-001 observed on 2009 November 18, the recorded detector temperature was the highest ($T = 45.13\,\mathrm{K}$) among all asteroid observations during Phase 3, and the correction factor was given as $f(T) = 0.954$. Then the flux density is scaled by $1/f(T) = 1.048$ to obtain the corrected value. This correction factor is assumed to not have wavelength-dependency. In the spectroscopic analysis, the flux and the wavelength accuracy strongly depend on the accuracy of the wavelength zero-point, which was estimated on the reference image of the N3 band. It was estimated to be, at worst, 1 pixel in our analysis. Thus, the flux and the wavelength uncertainties were estimated by calculating how much the spectrum changed when the wavelength zero-point was shifted by ± 1 pixel (Shimonishi et al. 2013).

Table 3. Observation log.*

Object	Obs ID†	Date‡ (UT)	r_h § [au]	Δ ‖ [au]	α ♯ [°]	ε ** [°]	APmag‡‡
1 Ceres	1520001-001	2008/11/29 15:47:13	2.556	2.357	22.7	90.1	8.37
1 Ceres	1520002-001	2008/11/29 17:26:04	2.556	2.356	22.7	90.2	8.36
2 Pallas	1520003-001	2008/09/02 12:20:53	2.479	2.262	24.0	90.1	9.06
2 Pallas	1520004-001	2008/09/02 20:35:12	2.478	2.258	24.0	90.3	9.05
4 Vesta	1520187-001	2009/01/24 00:42:44	2.561	2.360	22.6	90.2	7.97
4 Vesta	1520188-001	2009/01/24 02:21:36	2.561	2.361	22.6	90.2	7.98
5 Astraea	1520076-001	2009/04/25 13:49:28	2.948	2.770	20.0	90.0	12.41
5 Astraea	1520075-001	2009/04/25 15:28:19	2.948	2.770	20.0	90.1	12.41
6 Hebe	5125810-001	2008/05/04 05:49:11	2.735	2.548	21.6	89.7	10.86
6 Hebe	5125811-001	2008/05/04 07:28:03	2.735	2.549	21.6	89.6	10.86
7 Iris	1520077-001	2008/07/07 00:21:05	2.924	2.743	20.3	89.9	11.04
7 Iris	1520078-001	2008/07/07 01:59:56	2.924	2.744	20.3	89.9	11.04
8 Flora	1520079-001	2009/01/22 23:10:12	2.496	2.294	23.2	90.0	11.21
9 Metis	1521231-001	2010/01/14 01:06:24	2.425	2.220	23.9	89.8	11.03
9 Metis	1521232-001	2010/01/14 02:45:16	2.425	2.219	23.9	89.8	11.03
9 Metis	1521233-001‡‡	2010/01/14 12:38:25	2.426	2.215	23.9	90.1	11.02
10 Hygiea	1520005-001	2009/02/26 04:34:35	3.457	3.322	16.6	89.4	11.62
10 Hygiea	1520006-001	2009/02/26 06:13:27	3.457	3.323	16.6	89.4	11.62
13 Egeria	1520007-001	2009/05/21 01:56:54	2.424	2.204	24.7	89.9	11.52
13 Egeria	1520008-001	2009/05/21 03:35:45	2.424	2.204	24.7	89.9	11.52
16 Psyche	1520143-001	2009/05/04 15:18:10	2.828	2.641	20.9	90.1	11.23
16 Psyche	1520144-001	2009/05/04 16:57:01	2.828	2.640	20.9	90.1	11.23
21 Lutetia	1520157-001	2008/09/02 17:09:33	2.263	2.024	26.5	90.1	11.91
21 Lutetia	1520158-001	2008/09/02 18:48:24	2.263	2.024	26.5	90.1	11.91
22 Kalliope	1520146-001	2008/06/24 02:40:52	3.119	2.953	19.0	89.8	12.17
22 Kalliope	1520145-001	2008/06/24 05:58:34	3.119	2.955	19.0	89.7	12.17
24 Themis	1520009-001	2009/02/07 19:49:05	2.914	2.737	19.8	90.3	12.53
24 Themis	1520010-001	2009/02/07 21:27:57	2.914	2.736	19.8	90.4	12.53
33 Polyhymnia	1521246-001	2009/11/12 06:20:29	1.897	1.625	31.4	89.7	12.07
33 Polyhymnia	1521247-001	2009/11/12 11:17:03	1.898	1.627	31.4	89.6	12.07
33 Polyhymnia	1521248-001	2009/11/12 12:55:55	1.898	1.627	31.4	89.5	12.07
40 Harmonia	1520105-001	2009/04/11 01:24:02	2.336	2.112	25.4	89.9	11.63
40 Harmonia	1520106-001	2009/04/11 11:17:09	2.336	2.117	25.4	89.6	11.64
42 Isis	1520107-001	2009/05/25 02:17:26	1.915	1.625	31.9	90.0	11.35
42 Isis	1520108-001	2009/05/25 03:56:17	1.915	1.625	31.9	90.0	11.35
44 Nysa	1520189-001‡‡	2009/06/08 00:42:05	2.718	2.516	21.9	90.3	11.91
44 Nysa	1520190-001	2009/06/08 02:20:56	2.718	2.516	21.9	90.3	11.91
46 Hestia	1520169-001	2009/08/19 01:43:14	2.510	2.297	23.8	90.0	13.42
46 Hestia	1520170-001	2009/08/19 03:22:05	2.510	2.298	23.8	89.9	13.42
49 Pales	1521189-001	2009/12/04 03:57:45	2.445	2.233	23.8	90.2	12.60
49 Pales	1521190-001	2009/12/04 05:36:36	2.445	2.234	23.8	90.2	12.60
49 Pales	1521191-001‡‡	2009/12/04 10:33:10	2.444	2.236	23.8	90.0	12.61
50 Virginia	1520175-001	2009/01/11 01:18:17	1.986	1.729	29.7	89.8	13.21
50 Virginia	1520176-001	2009/01/11 02:57:09	1.986	1.729	29.7	89.8	13.21
51 Nemausa	1520019-001	2009/08/18 16:40:37	2.497	2.276	23.9	90.3	12.35
51 Nemausa	1520020-001	2009/08/18 18:19:28	2.496	2.275	23.9	90.4	12.35
52 Europa	1520021-001	2008/06/21 22:45:26	3.283	3.122	18.0	90.0	12.26
52 Europa	1520022-001	2008/06/22 00:24:17	3.283	3.121	18.0	90.1	12.26
55 Pandora	1521264-001	2009/11/18 05:40:38	2.389	2.175	24.4	90.0	12.42
55 Pandora	1521265-001	2009/11/18 10:37:13	2.389	2.178	24.4	89.8	12.42
55 Pandora	1521266-001	2009/11/18 12:16:04	2.389	2.179	24.4	89.8	12.42
56 Melete	1520171-001	2008/07/21 12:48:59	2.222	1.974	27.2	90.1	12.74
56 Melete	1520172-001	2008/07/21 14:27:50	2.222	1.973	27.2	90.1	12.74

Table 3. (Continued)

Object	Obs ID[†]	Date[‡] (UT)	r_h [§] [au]	Δ [‖] [au]	α [♯] [°]	ε [**] [°]	APmag[‡‡]
64 Angelina	1520191-001	2008/07/01 16:40:57	2.916	2.732	20.4	90.1	12.83
64 Angelina	1520192-001	2008/07/01 18:19:48	2.916	2.731	20.4	90.1	12.83
65 Cybele	1520167-001	2009/06/09 03:03:17	3.277	3.114	18.0	90.1	12.78
65 Cybele	1520168-001	2009/06/09 12:56:22	3.278	3.109	18.0	90.4	12.78
69 Hesperia	1520149-001	2008/07/11 20:31:05	3.109	2.936	19.1	90.1	12.77
79 Eurynome	1521249-001	2009/11/30 03:34:50	2.317	2.093	25.2	90.2	12.41
79 Eurynome	1521250-001	2009/11/30 11:49:08	2.317	2.089	25.2	90.4	12.41
79 Eurynome	1521251-001	2009/11/30 13:28:00	2.318	2.089	25.2	90.5	12.41
81 Terpsichore	1520029-001	2009/08/17 20:51:33	2.297	2.061	26.2	90.0	13.04
81 Terpsichore	1520030-001	2009/08/17 22:30:24	2.297	2.060	26.2	90.1	13.04
87 Sylvia	1520163-001	2009/02/12 16:46:27	3.617	3.477	15.8	90.1	13.30
87 Sylvia	1520164-001	2009/02/12 18:25:19	3.617	3.476	15.8	90.2	13.30
89 Julia	1521252-001	2010/01/13 01:19:25	2.222	1.991	26.3	90.1	11.02
89 Julia	1521253-001	2010/01/13 02:58:17	2.222	1.992	26.3	90.0	11.02
89 Julia	1521254-001	2010/01/13 04:37:08	2.222	1.993	26.3	90.0	11.02
92 Undina	1520179-001	2009/02/23 21:20:05	3.309	3.147	17.4	90.6	12.61
92 Undina	1520180-001	2009/02/23 22:58:56	3.309	3.146	17.4	90.6	12.61
94 Aurora	1520033-001	2008/08/29 17:33:42	2.891	2.708	20.4	90.1	13.05
94 Aurora	1520034-001	2008/08/29 19:12:33	2.891	2.707	20.4	90.1	13.05
106 Dione	1521201-001	2009/12/19 01:28:32	2.648	2.462	21.8	89.8	12.54
106 Dione	1521203-001	2009/12/19 04:46:15	2.648	2.464	21.8	89.7	12.54
106 Dione	1521202-001	2009/12/19 03:07:24	2.648	2.463	21.8	89.8	12.54
121 Hermione	1520035-001	2008/06/08 03:37:06	3.074	2.902	19.3	90.0	13.04
121 Hermione	1520036-001	2008/06/08 13:30:13	3.074	2.896	19.3	90.3	13.03
127 Johanna	1521342-001	2009/12/29 00:24:05	2.768	2.592	20.8	89.7	13.90
127 Johanna	1521343-001	2009/12/29 02:02:56	2.768	2.593	20.8	89.7	13.91
127 Johanna	1521344-001	2009/12/29 03:41:48	2.768	2.594	20.8	89.6	13.91
128 Nemesis	5125812-001	2008/05/03 15:48:42	2.693	2.494	22.0	90.2	12.69
128 Nemesis	5125813-001	2008/05/03 17:27:33	2.693	2.493	22.0	90.2	12.69
129 Antigone	1520147-001	2008/11/02 03:06:50	3.204	3.052	18.0	89.6	12.76
129 Antigone	1520148-001	2008/11/02 13:00:00	3.203	3.046	18.0	90.0	12.76
135 Hertha	1520159-001	2009/02/10 04:40:31	2.507	2.310	23.2	89.7	13.14
135 Hertha	1520160-001	2009/02/10 06:19:23	2.507	2.311	23.2	89.6	13.14
140 Siwa	1521268-001	2009/11/07 06:03:12	2.218	1.987	26.5	89.8	12.76
140 Siwa	1521269-001	2009/11/07 10:59:47	2.218	1.990	26.5	89.7	12.76
140 Siwa	1521267-001	2009/11/07 04:24:21	2.218	1.987	26.5	89.9	12.76
145 Adeona	1521210-001	2010/01/29 18:38:12	2.509	2.300	23.1	90.5	13.03
145 Adeona	1521211-001	2010/01/29 20:17:03	2.509	2.299	23.1	90.5	13.03
145 Adeona	1521212-001[‡‡]	2010/01/29 21:55:55	2.510	2.298	23.1	90.6	13.03
148 Gallia	1521258-001	2009/12/23 00:56:17	2.261	2.035	25.8	90.0	12.12
148 Gallia	1521259-001	2009/12/23 02:35:09	2.261	2.036	25.8	90.0	12.12
148 Gallia	1521260-001	2009/12/23 05:52:53	2.261	2.037	25.8	89.9	12.12
153 Hilda	1520213-001	2008/11/21 02:43:09	3.772	3.647	15.2	89.6	14.01
153 Hilda	1520214-001	2008/11/21 04:22:01	3.772	3.648	15.2	89.5	14.01
161 Athor	1520153-001	2009/06/20 12:34:09	2.061	1.792	29.6	90.0	13.31
161 Athor	1520154-001	2009/06/20 14:13:00	2.061	1.791	29.6	90.1	13.31
173 Ino	1521270-001	2010/01/08 00:53:31	2.224	1.991	26.2	90.2	12.32
173 Ino	1521271-001	2010/01/08 02:32:23	2.224	1.992	26.2	90.2	12.32
173 Ino	1521272-001	2010/01/08 04:11:15[‡]	2.224	1.993	26.2	90.2	12.32
185 Eunike	1521222-001	2010/01/15 23:12:14	3.083	2.921	18.6	90.1	13.35
185 Eunike	1521224-001	2010/01/16 02:29:57	3.083	2.919	18.6	90.2	13.35
185 Eunike	1521223-001	2010/01/16 00:51:06	3.083	2.920	18.6	90.1	13.35
216 Kleopatra	1520155-001	2008/06/08 21:38:33	2.444	2.222	24.5	90.1	11.93

Table 3. (Continued)

Object	Obs ID[†]	Date[‡] (UT)	r_h [§] [au]	Δ [‖] [au]	α [♯] [°]	ε [**] [°]	APmag[††]
216 Kleopatra	1520156-001	2008/06/09 02:35:07	2.444	2.219	24.6	90.2	11.92
216 Kleopatra	1521177-001	2009/11/24 12:30:53	2.666	2.465	21.7	90.7	12.27
246 Asporina	1520193-001	2008/12/24 00:47:07	2.702	2.513	21.4	90.2	13.82
246 Asporina	1520194-001	2008/12/24 02:25:59	2.702	2.512	21.4	90.3	13.82
250 Bettina	1520161-001[‡‡]	2008/12/14 09:15:33	3.086	2.924	18.6	90.1	13.31
250 Bettina	1520162-001	2008/12/14 10:54:25	3.086	2.925	18.6	90.0	13.31
308 Polyxo	1521261-001	2010/02/13 17:36:37	2.729	2.544	21.2	90.0	13.34
308 Polyxo	1521262-001	2010/02/14 00:12:02	2.729	2.541	21.2	90.2	13.34
308 Polyxo	1521263-001	2010/02/14 01:50:54	2.729	2.540	21.2	90.3	13.33
336 Lacadiera	1520199-001	2009/05/15 15:42:30	2.250	2.012	26.7	89.9	14.24
336 Lacadiera	1520200-001	2009/05/16 04:53:18	2.250	2.018	26.7	89.5	14.25
349 Dembowska	1520185-001	2008/12/04 12:46:59	3.051	2.885	18.8	90.1	11.37
349 Dembowska	1520186-001	2008/12/04 14:25:50	3.051	2.884	18.8	90.2	11.37
354 Eleonora	1520131-001	2008/07/13 12:07:19	3.045	2.865	19.5	90.3	11.88
354 Eleonora	1520132-001	2008/07/13 13:46:10	3.045	2.864	19.5	90.3	11.88
361 Bononia	1520209-001	2008/08/16 16:31:40	3.327	3.168	17.7	90.1	14.26
361 Bononia	1520210-001	2008/08/16 18:10:31	3.327	3.167	17.7	90.1	14.26
371 Bohemia	1520205-001	2009/06/12 01:02:13	2.666	2.471	22.4	89.7	13.89
371 Bohemia	1520206-001	2009/06/12 02:41:04	2.666	2.471	22.4	89.7	13.89
387 Aquitania	1521387-001	2010/01/03 00:35:40	2.795	2.614	20.6	90.2	12.75
387 Aquitania	1521388-001	2010/01/03 02:14:32	2.796	2.615	20.6	90.1	12.75
387 Aquitania	1521389-001	2010/01/03 05:32:15	2.796	2.617	20.6	90.0	12.75
419 Aurelia	1521363-001	2010/01/03 07:16:46	2.771	2.596	20.8	89.7	13.73
419 Aurelia	1521364-001	2010/01/03 08:55:37	2.771	2.598	20.8	89.6	13.73
419 Aurelia	1521365-001	2010/01/03 12:13:20	2.771	2.600	20.8	89.5	13.73
423 Diotima	1520060-001	2008/12/01 11:26:37	3.051	2.892	18.8	89.7	12.93
423 Diotima	1520059-001	2008/12/01 09:47:45	3.051	2.891	18.9	89.8	12.93
451 Patientia	1520061-001	2009/08/02 09:24:28	3.290	3.128	18.0	90.1	12.60
451 Patientia	1520062-001	2009/08/03 00:14:05	3.290	3.137	18.0	89.6	12.61
476 Hedwig	1520165-001	2008/08/14 01:05:10	2.480	2.266	24.1	89.9	13.42
476 Hedwig	1520166-001	2008/08/14 02:44:02	2.480	2.266	24.1	89.9	13.43
511 Davida	1520065-001	2008/11/16 11:26:35	2.662	2.469	21.8	90.2	11.35
511 Davida	1520066-001	2008/11/16 13:05:26	2.663	2.468	21.8	90.2	11.35
532 Herculina	1520139-001	2009/02/12 04:24:06	2.871	2.696	20.1	90.0	11.12
532 Herculina	1520140-001	2009/02/12 06:02:58	2.870	2.697	20.1	89.9	11.12
704 Interamnia	1520069-001	2008/12/09 03:17:00	3.348	3.200	17.1	90.0	12.21
704 Interamnia	1520070-001	2008/12/09 11:31:20	3.349	3.195	17.1	90.3	12.21
704 Interamnia	1521178-001	2010/02/08 20:43:09	3.502	3.349	16.4	90.6	12.38
773 Irmintraud	1520201-001	2009/07/08 13:46:01	2.727	2.542	21.9	89.3	14.36
773 Irmintraud	1520202-001	2009/07/08 15:24:52	2.727	2.541	21.9	89.4	14.36
4015 Wilson-Harrington	1521116-001	2009/11/18 13:57:26	1.059	0.379	69.0	90.0	16.43

*Note that r_h, Δ, α, ε, and APmag are calculated by the National Aeronautics and Space Administration (NASA) Jet Propulsion Laboratory (JPL) HORIZONS system ⟨https://ssd.jpl.nasa.gov/horizons.cgi⟩.

[†]152xxxx = SOSOS mission program observations, 520xxxx = Director's time observations.

[‡]Start time of one pointed observation sequence.

[§]Heliocentric distance to the object.

[‖]Geocentric distance to the object.

[♯]Solar phase angle (Sun–Target–Observer).

**Solar elongation angle (Sun–Observer–Target).

[††]Apparent visual magnitude calculated.

[‡‡]The data are not used for analyses due to contamination of ghost pattern or background stars.

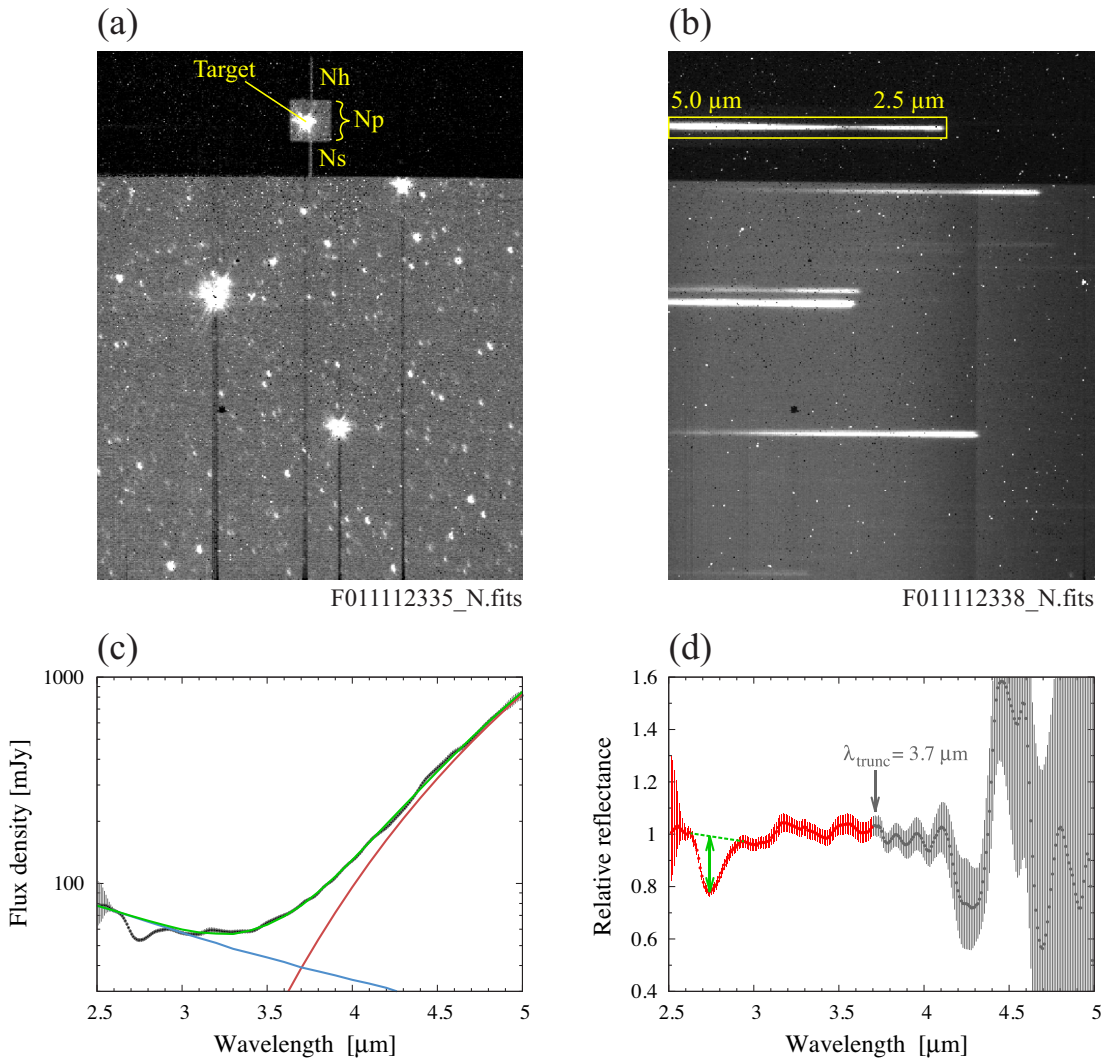

Fig. 3. Example of data reduction for C-type asteroid 511 Davida (Obs ID:1520065-001, observed on 2008 November 16). (a) Reference image in the N3 band, which is used to derive the wavelength reference position in the spectral images. (b) Spectroscopic image with the grism (NG). One pointed observation consists of four spectroscopic frames, one reference frame, and four or five spectroscopic frames (total number of frames depends on the attitude stability of the satellite). The target is placed on the $1' \times 1'$ Np window to avoid contamination from background stars. (c) Spectrum extracted from the target using the toolkit. The red, blue, and green curves denote the thermal component of the spectrum calculated by the NEATM that is removed to derive the reflectance spectrum, the spectrum of the reflected sunlight component, and the total modeled spectrum, respectively. (d) Reflectance spectrum normalized at 2.6 μm. The spectrum beyond the truncated wavelength ($\lambda_{\rm trunc}$) cannot be used due to the uncertainty of the thermal model (see sub-subsection 2.2.4). The green dotted line denotes the continuum and the arrow shows the point where the band depth is measured. (Color online)

Finally, one-dimensional spectra were extracted from the two-dimensional images by summing signals over 7 pixels (approximately 10.″5) in the spatial direction to reduce the effect of hot pixels and/or cosmic rays that hit the detector. Then, one-dimensional spectra were extracted. The obtained one-dimensional spectra were smoothed along their wavelength with 5 pixels (i.e., $1.5\times$ PSF) for further analyses. In this study, we focus on broader features (bandwidth of $>0.1\,\mu$m) that appeared at around 2.7 μm and 3.1 μm in the spectra (cf. table 1 in Rivkin et al. 2015a). There are wavy patterns in other wavelengths remaining in some extracted spectra, which have not been seen in meteorite spectra. It is likely that most of them are spurious due to the contamination of neighboring stars or insufficient background subtraction, although we cannot completely rule out that they are real features. In the following, we do not discuss other features. The obtained spectra of each pointed observation are summarized in the supplementary data section available in the online edition.

After visual inspection, it was found that some observational data were contaminated by ghost patterns (Egusa et al. 2016) or by nearby stars that happened to be in the same field of the Np window. The data of the following observations were therefore removed from further analyses

(see table 3): Obs ID:1521233-001 for 9 Metis, Obs ID: 1520189-001 for 44 Nysa, Obs ID:1521191-001 for 49 Pales, Obs ID:1521212-001 for 145 Adeona, and Obs ID:1520161-001 for 250 Bettina.

2.2.2 Instrument linearity and saturation

Saturation of the observed signal causes severe problems in the cases of larger asteroids, which need to be handled with care. The saturation level of the detector during Phase 3 observations was reported as 2000 ADU per pixel (Onaka et al. 2008; see also the IRC Data User Manual), which roughly corresponds to ~1 Jy for the grism mode. A brighter observed flux than this value cannot be assured in the linearity correction of the detector. This was the case for the largest objects: 1 Ceres, 2 Pallas, and 4 Vesta. In this work, the following empirical method was used to determine the available wavelength range and extract the spectra.

The minimum observation unit of the IRC is called the exposure cycle, which consists of one short exposure (~4.6 s) and one long exposure (~44.4 s) for the near-infrared channel. One pointed observation of spectroscopy contains 8–9 exposure cycles, as described in subsection 2.1. Short- and long-exposure data are reduced separately by the toolkit with each set of the calibration parameters. Unusual behaviors due to non-linearity or saturation of the detector can be found by comparing short- and long-exposure spectra. Figure 4 shows the short- and long-exposure spectra of 1 Ceres, 2 Pallas, and 4 Vesta. Comparison of the short- and long-exposure spectra suggests that the available wavelength range in which both spectra match to an accuracy of 10% of each flux is $\lambda < 3.7\,\mu$m for 1 Ceres and $\lambda < 3.75\,\mu$m for 2 Pallas. The spectra within these wavelengths can be used for further analyses. However, for 4 Vesta, the short- and long-exposure spectra agree only within $3.2 < \lambda < 3.5\,\mu$m, which does not provide the information necessary for the present study. Thus, the 4 Vesta spectra cannot be used for further analyses.

The spectra of the other asteroids do not display such unusual behavior. Specifically, the reduced reflectance spectra (described below) of 1 Ceres and 2 Pallas are consistent with the literature (Rivkin 1997; Rivkin et al. 2003, 2006b; Vernazza et al. 2005; Rivkin & Volquardsen 2010; de Sanctis et al. 2015; Takir et al. 2015b).

2.2.3 Thermal component subtraction

The spectrum obtained in the previous section essentially consisted of two components in the wavelength range of 2.5–5 μm: thermal emission of the asteroid itself (F_e) and reflected sunlight (F_r). To obtain the reflectance spectrum, it was necessary to remove the thermal component from the spectrum, which depends on the distribution of surface temperature at the epoch of the observation. In this work, the Near-Earth Asteroid Thermal Model (NEATM; Harris 1998) was used to calculate the thermal flux at longer wavelengths by fitting the spectrum. NEATM is a refinement of the standard thermal model (STM; Lebofsky et al. 1986). NEATM solves simultaneously for the diameter (D) and the geometric albedo (p_v) as well as the beaming parameter (η) to fit the observed (infrared) flux. η was originally introduced in the STM to allow the model temperature distribution to fit the observed enhancement of thermal emission at small solar phase angles (e.g., Lebofsky et al. 1986). In practice, η can be treated as a model parameter that allows a first-order correction for any effect that influences the observed surface temperature distribution. The geometric information; i.e., the heliocentric distance (r_h), the geocentric distance (Δ), and the phase angle (α), were obtained from JPL Horizons (table 3). The absolute magnitude (H) and the slope parameter (G) were employed as the visible flux (Bowell et al. 1989). The emissivity was assumed to be constant at $\epsilon = 0.9$ throughout the wavelengths considered in this study (cf. Lebofsky et al. 1986). D and η were parameterized to fit the thermal flux of the asteroid. After subtracting the thermal component fitted by NEATM, the spectrum was divided by the solar spectrum based on the corrected Kurucz model (Berk et al. 1999) to obtain the reflectance spectrum of the asteroid. The obtained reflectance spectra of each pointed observation are summarized in the supplementary data section available in the online edition.

2.2.4 Criterion to reject spectra severely contaminated by thermal emission

In this research, we aimed to detect small absorption features (~10%) on the spectrum of the reflected sunlight component. The thermal component of the spectra was subtracted as described in the previous section. However, it was still necessary to carefully handle the "contamination" of thermal emission from the asteroid itself. It is hard to extract reflectance spectra with a sufficient S/N ratio from spectra with large thermal emission contribution.

The grism spectroscopy of the AKARI/IRC covers a wavelength range of 2.5–5 μm. At these wavelengths, thermal emission has an equivalent contribution to the total spectrum of a main-belt asteroid to the reflected component. As mentioned above, thermal emission was estimated by NEATM; that is, thermal emission was assumed as a graybody with a fixed emissivity of $\epsilon = 0.9$. Realistically, the emissivity is not necessarily constant. This ambiguity of emissivity could affect the detailed features of the reflectance spectrum. We examined the contribution of the thermal component in the total flux density as follows.

Let us consider the relationship between the bihemispherical reflectivity (p_h) and the hemispherical

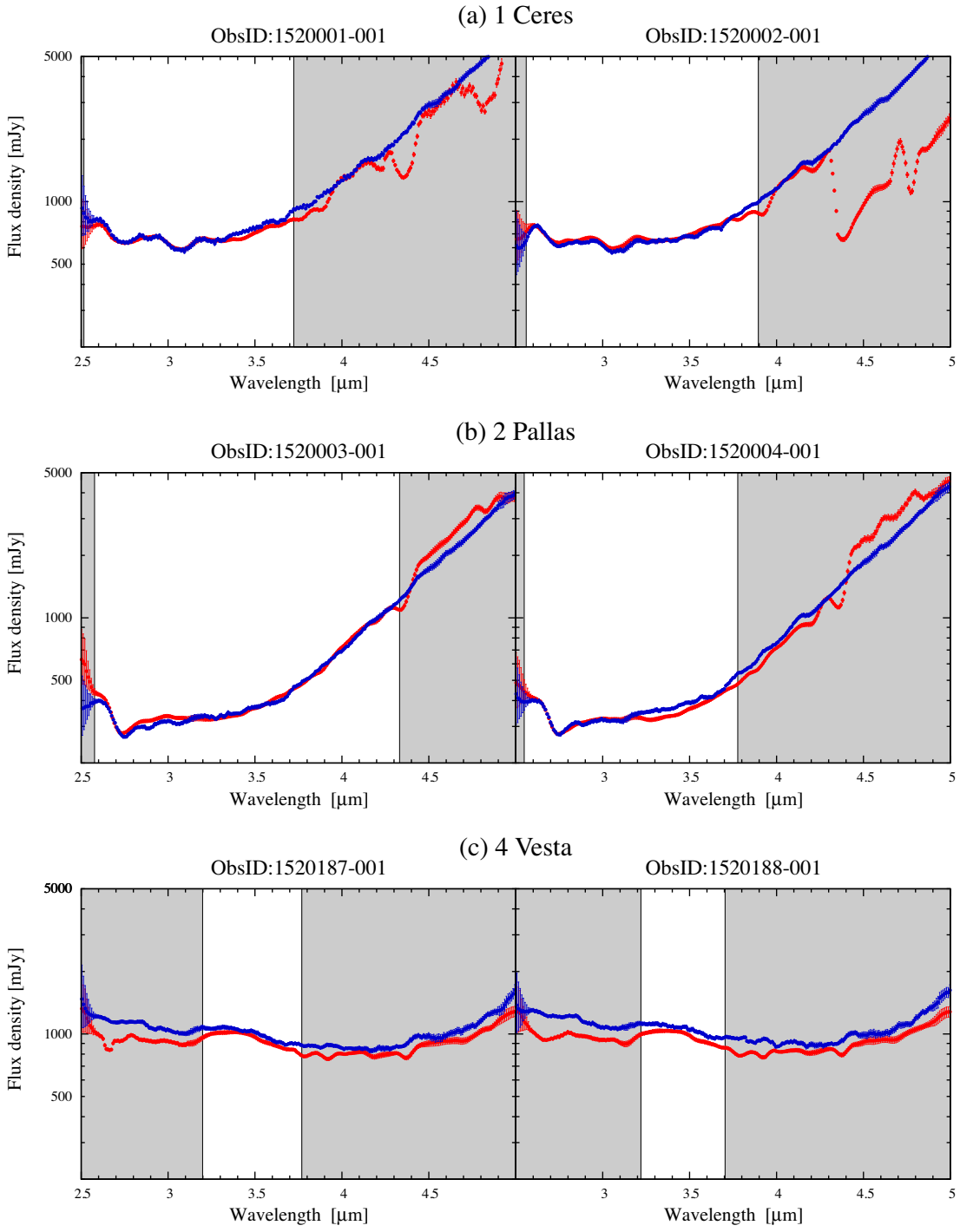

Fig. 4. AKARI IRC 2.5–5.0 μm spectra of 1 Ceres, 2 Pallas, and 4 Vesta of each pointed observation. The red and blue dots denote the long-exposure and short-exposure data, respectively. The gray region denotes the unreliable wavelength range determined by inconsistency between the long- and short-exposure data. (Color online)

emissivity ($\varepsilon_{\rm h}$) at a certain wavelength. As stated by Kirchhoff's law of thermal radiation, $p_{\rm h}$ and $\varepsilon_{\rm h}$ are complementary as (Hapke 1993)

$$\varepsilon_{\rm h} = 1 - p_{\rm h}. \quad (2)$$

Note that both $p_{\rm h}$ and $\varepsilon_{\rm h}$ have wavelength dependency; $p_{\rm h} = p_{\rm h}(\lambda)$, and $\varepsilon_{\rm h} = \varepsilon_{\rm h}(\lambda)$. We assume that the spectrum has an absorption feature with a band depth of s. Here, the band depth is defined as a fraction of the depression from the continuum. The bi-directional reflectivity to be observed

with the absorption feature (p_d) is given as

$$p_d = p_{d0}(1 - s), \tag{3}$$

where p_{d0} is the continuum of the bi-directional reflectivity. In the same way, we assume that the spectrum has an *emission* feature with an emission strength of e. The directional emissivity to be observed with the emission feature (ε_d) is given as

$$\varepsilon_d = \varepsilon_{d0}(1 + e), \tag{4}$$

where ε_{d0} is the continuum of the directional emissivity. It is assumed that an absorption feature appears as downward from the continuum, while an emission feature appears as upward. Therefore, an absorption is denoted negative ($-s$) in equation (3) and an emission is positive ($+e$) in equation (4). The bi-hemispherical reflectivity (p_h) and the bi-directional reflectivity (p_d) are assumed to have the same relation as the Bond albedo to the geometric albedo in the IAU H–G function model (Bowell et al. 1989) as

$$p_h = q\, p_d, \tag{5}$$

where q is the phase integral empirically given by the slope parameter (G) as:

$$q = 0.290 + 0.684G. \tag{6}$$

It should be noted that the applicability of the H–G function in the infrared wavelengths is not well studied. Lederer et al. (2008) reported the photometric properties of S-type asteroid 25143 Itokawa based on ground-based *UBVRIJHK* broad-band observational data (0.36–2.15 μm); the difference of the phase integral by wavelength is small ($q = 0.11 \pm 0.01$ in the V band; 0.13 ± 0.01 in the K band). There are no other reports to-date of the phase integral measured in the near-infrared wavelengths. Here the wavelength difference of the phase integral of asteroids observed in this study is assumed to be small. Thus equations (5)–(6) is applied to all asteroids in our analysis.

In addition, the angular variation of the directional emissivity (ε_d) is assumed to be neglected (e.g., Sobrino & Cuenca 1999; García-Santos et al. 2012), thus to be identical to the hemispherical emissivity (ε_h) as

$$\varepsilon_h \simeq \varepsilon_d \tag{7}$$

and

$$\varepsilon_{h0} \simeq \varepsilon_{d0}, \tag{8}$$

where ε_{h0} is the continuum of the hemispherical emissivity, given by Kirchhoff's law as

$$\varepsilon_{h0} = 1 - p_{h0}, \tag{9}$$

where p_{h0} is the continuum of the bi-hemispherical reflectivity, and again

$$p_{h0} = q\, p_{d0}. \tag{10}$$

From these equations,

$$(1 - q\, p_{d0})(1 + e) = 1 - q\, p_{d0}(1 - s). \tag{11}$$

Thus, we have

$$\frac{e}{s} = \frac{q\, p_{d0}}{1 - q\, p_{d0}}. \tag{12}$$

An asteroid spectrum (F_{tot}) comprises two components: reflected sunlight (F_r) and thermal emission (F_e):

$$F_{tot} = F_r + F_e. \tag{13}$$

Flux densities of the absorption feature (ΔF_r) and emission feature (ΔF_e) are written as

$$|\Delta F_r| = s F_r, \tag{14}$$

$$|\Delta F_e| = e F_e. \tag{15}$$

To detect the absorption feature (i.e., measuring s) with more than $x \times 100\%$ accuracy, the contribution of the emission feature of the thermal component should be suppressed as

$$\left|\frac{\Delta F_e}{\Delta F_r}\right| < x, \tag{16}$$

thus

$$\frac{F_e}{F_r} < x\frac{1 - q\, p_{d0}}{q\, p_{d0}} \quad \text{or} \quad \frac{F_e}{F_{tot}} < \frac{1}{[q\, p_{d0}/x(1 - q\, p_{d0})] + 1}. \tag{17}$$

Here, we consider that x is the same value as the typical uncertainty of the flux density of AKARI spectroscopy.

The geometric infrared albedo (p_{IR}) is defined as the ratio of the brightness at zero phase angle to the brightness of a perfect Lambert disk of the equivalent radius at a given infrared wavelength. We assume that the bi-directional reflectivity of the continuum (p_{d0}) is equal to the infrared albedo (p_{IR}) at 2.45 μm which is given as

$$p_{d0} = p_{IR} \simeq p_v \frac{R_{2.45}}{R_{0.55}}, \tag{18}$$

where p_v, $R_{2.45}$, and $R_{0.55}$ are the geometric visible albedo, the relative reflectance at 2.45 μm, and the relative reflectance at 0.55 μm, respectively. Note that the second equal sign of equation (18) comes from the assumption that the ratio of the geometric infrared albedo to the geometric visible albedo is the same as the ratio of the relative reflectance at 2.45 μm and that at 0.55 μm. The relative reflectance values at 0.55 μm and 2.45 μm are obtained from the vis-NIR spectra (spectral data are compiled by Hasegawa et al. 2017).

F_e/F_{tot}, which can be calculated by the thermal model described in the previous subsection, is a function of wavelength. Thus, equation (17) with $x = 0.04$ (i.e., 4% uncertainty; see subsection 3.1) is treated as a condition of the available wavelength range (upper limit of wavelength, λ_{trunc}) to extract the reflectance spectrum with sufficient accuracy. λ_{trunc} values for each observed target are listed in table 4. It is natural that 4015 Wilson-Harrington, which is the near-Earth object, has a high surface temperature; thus, the thermal component fully occupies the wavelength coverage of the spectroscopy ($\lambda_{trunc} = 3.0$ μm). We cannot retrieve any valid reflectance spectra from this object; instead, the spectral data of this object were utilized for studying the thermal properties of the asteroid (e.g., Bach et al. 2017).

2.2.5 3 μm-band depth measurements

The measurement method for band depth described in Takir and Emery (2012) cannot be applied to our data set because our spectra only cover wavelengths longer than 2.5 μm, which is the starting wavelength for absorption features associated with hydrated minerals. Instead, the band depth ($\mathcal{D}$) was measured as follows.

(1) Before measuring the band depth, two or three reflectance spectra of each asteroid were averaged.
(2) The continuum (R_c) was defined as the connection of two local peaks of the reflectance spectrum across the peak wavelength of the absorption feature.
(3) The band depth ($\mathcal{D}$) was defined as (see figure 3)

$$\mathcal{D} = \max\left(\frac{R_c - R_\lambda}{R_c}\right), \quad (19)$$

where R_λ is the reflectance spectrum (cf. Clark & Roush 1984).

The peak wavelength was defined as the wavelength with the maximum value of the band depth. To increase the S/N, two or three spectra obtained were averaged in step (1). Thus, the spectral variability due to heterogeneities of the surface material or any other reason was smoothed out. After a visual inspection of our results, obvious features appeared at around 2.7 μm and 3.1 μm in the spectra. Thus, two band depths, $\mathcal{D}_{2.7}$ and $\mathcal{D}_{3.1}$, are treated as absorption features in this study and small features in other wavelengths are not considered.

3 Results

3.1 General trend of spectra

The obtained reflectance spectra are summarized in figures 5–8.

Figure 9 shows the distribution of uncertainties of all the data points in the reflectance spectra of 64 asteroids. Most of the data points in the reflectance spectra have uncertainties smaller than 10% (the median value is 3.8%). The uncertainties in the reflectance spectra are caused by the uncertainty in the absolute flux calibration (~5%), the ambiguity of the wavelength zero-point on the reference image (~8%), and the fluctuation of the sky background (~3%), which are described in sub-subsection 2.2.1. Uncertainty in the thermal model calculation described in sub-subsection 2.2.3 is not taken into account in the reflectance spectra; this uncertainty contributes to the spectra at λ_{trunc} or longer wavelengths.

As described above, the observed spectrum of 4 Vesta (V-type) is saturated in the 3 μm band (sub-subsection 2.2.2), and the thermal contamination of 4015 Wilson-Harrington (B-type) is not fully corrected (sub-subsection 2.2.4). Therefore, the spectra of these two objects cannot be used for further analysis. In total, the reflectance spectra of 64 objects are available in this study.

Diagnostic spectral features appear at wavelengths from 2.6 μm to 2.9 μm or longer with a band center of ~2.75 μm (hereafter the 2.7 μm band), and from 2.8–2.9 μm to 3.2 μm or longer with a band center of ~3.05 μm (hereafter the 3.1 μm band). Our results confirm that no significant spectral feature with a broad peak centered at 2.95 μm is found in the asteroid spectra, while such a feature sometimes appears in the spectra of meteorites, which is attributed to adsorbed water (Beck et al. 2010; Rivkin et al. 2015a). There are other absorption features in the 3 μm band; for example, those associated with organic materials at 3.4–3.6 μm (e.g., De Sanctis et al. 2017), which is another aspect of interest to this study.

Most C-complex asteroids have clear absorption features in the 2.7 μm band, as well as some in the 3.1 μm band. On the contrary, most S-complex asteroids show no significant features at these wavelengths. Some X-complex asteroids have absorption features in the 2.7 μm band, but among D-complex asteroids, only one asteroid in our data shows an absorption feature in the 2.7 μm band.

The band depths and the peak wavelengths of spectra in the 2.7 and 3.1 μm bands for each asteroid are summarized in table 5. The 3 μm band shape in this table is determined

Table 4. Criteria for thermal contamination (see sub-subsection 2.2.4 for details).

Object	Obs ID	$(R_{2.45}/R_{0.55})^*$	$p_{d0}{}^\dagger$	max $(F_e/F_{tot})^\ddagger$	λ_{trunc} [μm]§
1 Ceres	1520001-001	1.014	0.088	0.5217	3.72
1 Ceres	1520002-001	1.014	0.088	0.5217	3.71
2 Pallas	1520003-001	0.845	0.127	0.4326	3.60
2 Pallas	1520004-001	0.845	0.127	0.4326	3.60
4 Vesta	1520187-001	1.161	0.397	0.1275	3.70
4 Vesta	1520188-001	1.161	0.397	0.1275	3.67
5 Astraea	1520076-001	1.332	0.350	0.1883	4.00
5 Astraea	1520075-001	1.332	0.350	0.1883	3.96
6 Hebe	5125810-001	1.285	0.306	0.1865	3.98
6 Hebe	5125811-001	1.285	0.306	0.1865	3.99
7 Iris	1520077-001	1.292	0.231	0.2703	4.11
7 Iris	1520078-001	1.292	0.231	0.2703	4.14
8 Flora	1520079-001	1.608	0.378	0.1426	3.77
9 Metis	1521231-001	1.542	0.329	0.1937	3.56
9 Metis	1521232-001	1.542	0.329	0.1937	3.54
9 Metis	1521233-001	1.542	0.329	0.1937	3.57
10 Hygiea	1520005-001	1.225	0.081	0.5302	4.29
10 Hygiea	1520006-001	1.225	0.081	0.5302	4.32
13 Egeria	1520007-001	1.099	0.095	0.4898	3.71
13 Egeria	1520008-001	1.099	0.095	0.4898	3.73
16 Psyche	1520143-001	1.560	0.282	0.2126	4.21
16 Psyche	1520144-001	1.560	0.282	0.2126	4.24
21 Lutetia	1520157-001	1.125	0.204	0.3154	3.57
21 Lutetia	1520158-001	1.125	0.204	0.3154	3.58
22 Kalliope	1520146-001	1.543	0.369	0.1627	3.89
22 Kalliope	1520145-001	1.543	0.369	0.1627	3.88
24 Themis	1520009-001	1.103	0.093	0.4775	3.95
24 Themis	1520010-001	1.103	0.093	0.4775	4.01
33 Polyhymnia	1521246-001	1.197	0.278	0.1812	3.31
33 Polyhymnia	1521247-001	1.197	0.278	0.1812	3.36
33 Polyhymnia	1521248-001	1.197	0.278	0.1812	3.33
40 Harmonia	1520105-001	1.308	0.305	0.2139	3.74
40 Harmonia	1520106-001	1.308	0.305	0.2139	3.78
42 Isis	1520107-001	1.392	0.220	0.2814	3.40
42 Isis	1520108-001	1.392	0.220	0.2814	3.40
44 Nysa	1520189-001	1.041	0.499	0.0789	4.79
44 Nysa	1520190-001	1.041	0.499	0.0789	4.59
46 Hestia	1520169-001	1.291	0.071	0.6059	3.77
46 Hestia	1520170-001	1.291	0.071	0.6059	3.82
49 Pales	1521189-001	0.979	0.060	0.6065	3.70
49 Pales	1521190-001	0.979	0.060	0.6065	3.74
49 Pales	1521191-001	0.979	0.060	0.6065	3.73
50 Virginia	1520175-001	1.038	0.052	0.6400	3.44
50 Virginia	1520176-001	1.038	0.052	0.6400	3.44
51 Nemausa	1520019-001	1.279	0.120	0.4612	3.90
51 Nemausa	1520020-001	1.279	0.120	0.4612	3.85
52 Europa	1520021-001	1.326	0.057	0.6054	4.32
52 Europa	1520022-001	1.326	0.057	0.6054	4.30
55 Pandora	1521264-001	1.470	0.495	0.1329	3.67
55 Pandora	1521265-001	1.470	0.495	0.1329	3.67
55 Pandora	1521266-001	1.470	0.495	0.1329	3.70
56 Melete	1520171-001	1.302	0.099	0.4779	3.47
56 Melete	1520172-001	1.302	0.099	0.4779	3.52
64 Angelina	1520191-001	1.231	0.634	0.0543	5.00
64 Angelina	1520192-001	1.231	0.634	0.0543	5.00

Table 4. (Continued)

Object	Obs ID	$(R_{2.45}/R_{0.55})^*$	$p_{d0}{}^\dagger$	max $(F_e/F_{tot})^\ddagger$	λ_{trunc} [μm]§
65 Cybele	1520167-001	1.351	0.059	0.6731	4.33
65 Cybele	1520168-001	1.351	0.059	0.6731	4.35
69 Hesperia	1520149-001	1.539	0.242	0.2468	4.40
79 Eurynome	1521249-001	1.322	0.276	0.2022	3.69
79 Eurynome	1521250-001	1.322	0.276	0.2022	3.78
79 Eurynome	1521251-001	1.322	0.276	0.2022	3.77
81 Terpsichore	1520029-001	1.201	0.058	0.6151	3.51
81 Terpsichore	1520030-001	1.201	0.058	0.6151	3.49
87 Sylvia	1520163-001	1.541	0.066	0.5807	4.42
87 Sylvia	1520164-001	1.541	0.066	0.5807	4.39
89 Julia	1521252-001	1.550	0.291	0.2226	3.56
89 Julia	1521253-001	1.550	0.291	0.2226	3.67
89 Julia	1521254-001	1.550	0.291	0.2226	3.60
92 Undina	1520179-001	1.314	0.361	0.1828	4.42
92 Undina	1520180-001	1.314	0.361	0.1828	4.37
94 Aurora	1520033-001	1.391	0.074	0.5538	3.81
94 Aurora	1520034-001	1.391	0.074	0.5538	3.82
106 Dione	1521201-001	1.015	0.085	0.5164	3.73
106 Dione	1521203-001	1.015	0.085	0.5164	3.79
106 Dione	1521202-001	1.015	0.085	0.5164	3.75
121 Hermione	1520035-001	1.203	0.070	0.5677	4.00
121 Hermione	1520036-001	1.203	0.070	0.5677	4.02
127 Johanna	1521342-001	1.226	0.080	0.5339	3.92
127 Johanna	1521343-001	1.226	0.080	0.5339	3.88
127 Johanna	1521344-001	1.226	0.080	0.5339	3.79
128 Nemesis	5125812-001	1.142	0.067	0.5766	3.81
128 Nemesis	5125813-001	1.142	0.067	0.5766	3.82
129 Antigone	1520147-001	1.440	0.266	0.1885	4.35
129 Antigone	1520148-001	1.440	0.266	0.1885	4.41
135 Hertha	1520159-001	1.460	0.250	0.2540	3.89
135 Hertha	1520160-001	1.460	0.250	0.2540	3.88
140 Siwa	1521268-001	1.307	0.088	0.5096	3.59
140 Siwa	1521269-001	1.307	0.088	0.5096	3.61
140 Siwa	1521267-001	1.307	0.088	0.5096	3.60
145 Adeona	1521210-001	1.126	0.056	0.6208	3.75
145 Adeona	1521211-001	1.126	0.056	0.6208	3.77
145 Adeona	1521212-001	1.126	0.056	0.6208	3.82
148 Gallia	1521258-001	1.440	0.346	0.1908	3.55
148 Gallia	1521259-001	1.440	0.346	0.1908	3.63
148 Gallia	1521260-001	1.440	0.346	0.1908	3.65
153 Hilda	1520213-001	1.428	0.097	0.4828	4.18
153 Hilda	1520214-001	1.428	0.097	0.4828	4.17
161 Athor	1520153-001	1.181	0.275	0.2412	3.33
161 Athor	1520154-001	1.181	0.275	0.2412	3.35
173 Ino	1521270-001	1.265	0.075	0.6201	3.52
173 Ino	1521271-001	1.265	0.075	0.6201	3.50
173 Ino	1521272-001	1.265	0.075	0.6201	3.51
185 Eunike	1521222-001	1.294	0.074	0.5537	4.04
185 Eunike	1521224-001	1.294	0.074	0.5537	4.08
185 Eunike	1521223-001	1.294	0.074	0.5537	4.15
216 Kleopatra	1520155-001	1.491	0.222	0.2331	4.01
216 Kleopatra	1520156-001	1.491	0.222	0.2331	4.05
216 Kleopatra	1521177-001	1.491	0.222	0.2331	4.03
246 Asporina	1520193-001	1.956	0.346	0.1904	4.19
246 Asporina	1520194-001	1.956	0.346	0.1904	4.20

Table 4. (Continued)

Object	Obs ID	$(R_{2.45}/R_{0.55})^*$	$p_{d0}{}^\dagger$	max $(F_e/F_{tot})^\ddagger$	λ_{trunc} [μm]§
250 Bettina	1520161-001	1.499	0.213	0.2887	4.65
250 Bettina	1520162-001	1.499	0.213	0.2887	4.74
308 Polyxo	1521261-001	1.641	0.085	0.4906	3.95
308 Polyxo	1521262-001	1.641	0.085	0.4906	3.99
308 Polyxo	1521263-001	1.641	0.085	0.4906	4.00
336 Lacadiera	1520199-001	1.413	0.066	0.5802	3.67
336 Lacadiera	1520200-001	1.413	0.066	0.5802	3.69
349 Dembowska	1520185-001	1.639	0.454	0.1016	4.29
349 Dembowska	1520186-001	1.639	0.454	0.1016	4.32
354 Eleonora	1520131-001	2.156	0.455	0.1013	4.04
354 Eleonora	1520132-001	2.156	0.455	0.1013	4.09
361 Bononia	1520209-001	1.933	0.077	0.5417	4.15
361 Bononia	1520210-001	1.933	0.077	0.5417	4.12
371 Bohemia	1520205-001	1.281	0.355	0.1861	3.99
371 Bohemia	1520206-001	1.281	0.355	0.1861	3.92
387 Aquitania	1521387-001	1.314	0.229	0.2728	4.01
387 Aquitania	1521388-001	1.314	0.229	0.2728	4.02
387 Aquitania	1521389-001	1.314	0.229	0.2728	4.01
419 Aurelia	1521363-001	1.155	0.059	0.6097	3.88
419 Aurelia	1521364-001	1.155	0.059	0.6097	3.85
419 Aurelia	1521365-001	1.155	0.059	0.6097	3.80
423 Diotima	1520060-001	1.319	0.065	0.5870	3.96
423 Diotima	1520059-001	1.319	0.065	0.5870	3.97
451 Patientia	1520061-001	1.230	0.087	0.4929	4.22
451 Patientia	1520062-001	1.230	0.087	0.4929	4.18
476 Hedwig	1520165-001	1.357	0.075	0.5507	3.70
476 Hedwig	1520166-001	1.357	0.075	0.5507	3.69
511 Davida	1520065-001	1.281	0.090	0.4989	3.70
511 Davida	1520066-001	1.281	0.090	0.4989	3.69
532 Herculina	1520139-001	1.344	0.247	0.2204	4.02
532 Herculina	1520140-001	1.344	0.247	0.2204	3.98
704 Interamnia	1520069-001	1.118	0.084	0.6094	4.34
704 Interamnia	1520070-001	1.118	0.084	0.6094	4.30
704 Interamnia	1521178-001	1.118	0.084	0.6094	4.29
773 Irmintraud	1520201-001	1.589	0.084	0.5197	3.90
773 Irmintraud	1520202-001	1.589	0.084	0.5197	3.90
4015 Wilson-Harrington	1521116-001	0.792	0.036	0.7182	3.00

*Ratio of the relative reflectance at 2.45 μm to that at 0.55 μm.
†The bi-directional reflectivity (assumed as same as the infrared albedo; see text).
‡Maximum ratio of the thermal emisson to the total flux density.
§Truncated wavelength for valid reflectance spectrum range.

by a combination of the spectral features in 2.7 μm ($\mathcal{D}_{2.7}$) and 3.1 μm ($\mathcal{D}_{3.1}$) bands as:

- **sharp** spectral features with only $\mathcal{D}_{2.7}$,
- **w-shape** spectral features with both $\mathcal{D}_{2.7}$ and $\mathcal{D}_{3.1}$,[4]
- **3 μm dent** features with only $\mathcal{D}_{3.1}$, or
- unclassified.

Here, detection of the band depth is identified by $S/N > 2$. The number of classified objects is summarized in figure 10; sharp (×23), w-shape (×4), and 3 μm dent (×8) out of 64 asteroids. The relationships between band depth and other physical parameters are shown in figures 11–19.

Figure 11 shows the relationship between the band depth in the 2.7 μm band and the geometric albedo. From this figure, a general trend of absorption in the 2.7 μm band is observed, whereby most C-complex asteroids (17 out of 22), three X-complex asteroids, and one D-complex asteroid have significant absorption features, which is typically associated with hydrated minerals. All these objects have low albedo ($p_v < 0.1$), except for 2 Pallas ($p_v = 0.15$; B-type). However, removing the top three

[4] Note that "w"-shape in this work is determined by the appearance of its spectrum, and is not intended to relate to "W"-class (wet M-class) asteroids (Rivkin et al. 1995, 2000).

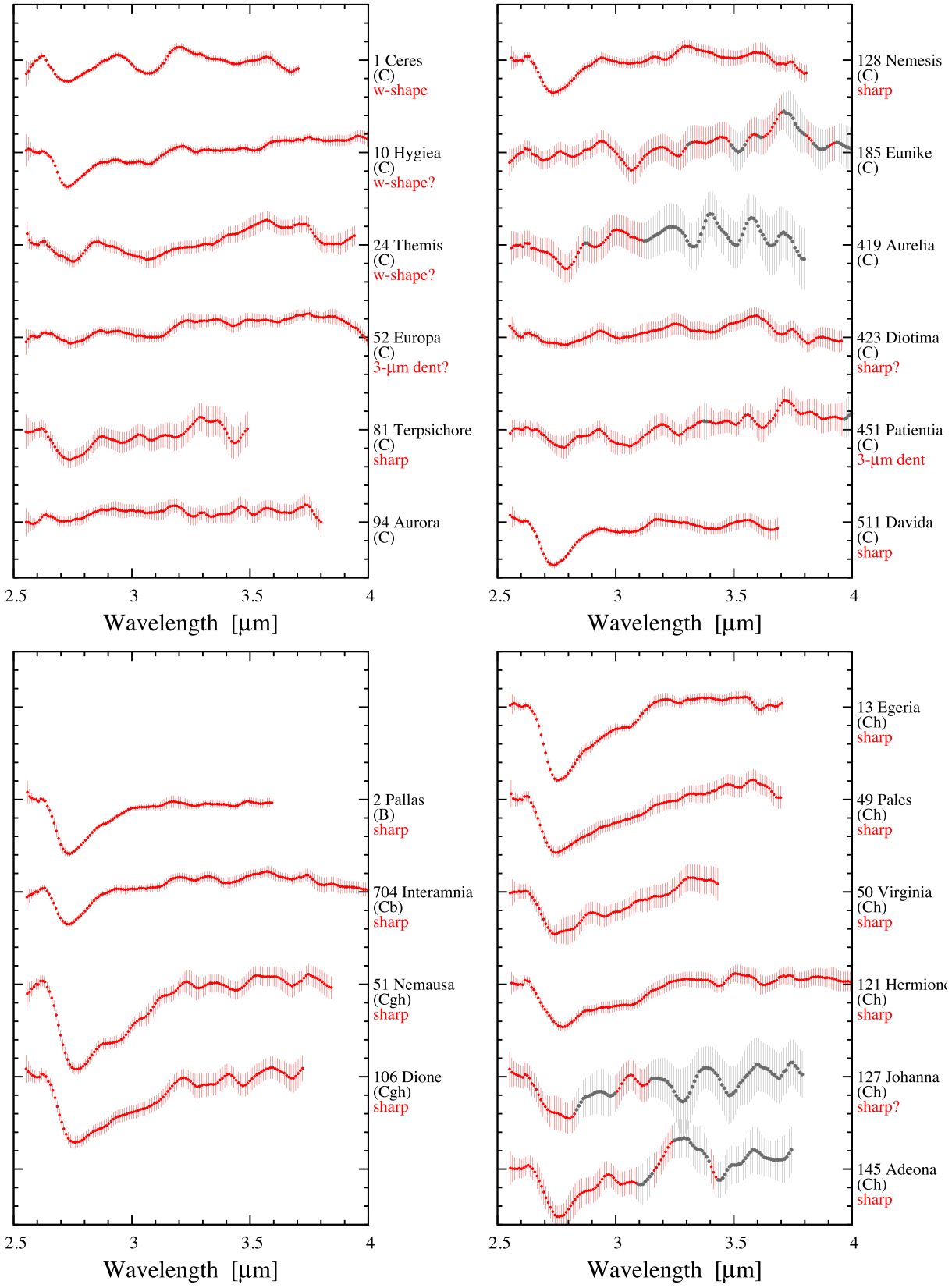

Fig. 5. Average reflectance spectra of C-complex asteroids. The Bus–DeMeo taxonomy is indicated in parentheses (see table 2). The gray dots indicate the unreliable wavelength region due to large uncertainties (>10%). The 3 μm band shape is given in red text (see table 5). (Color online)

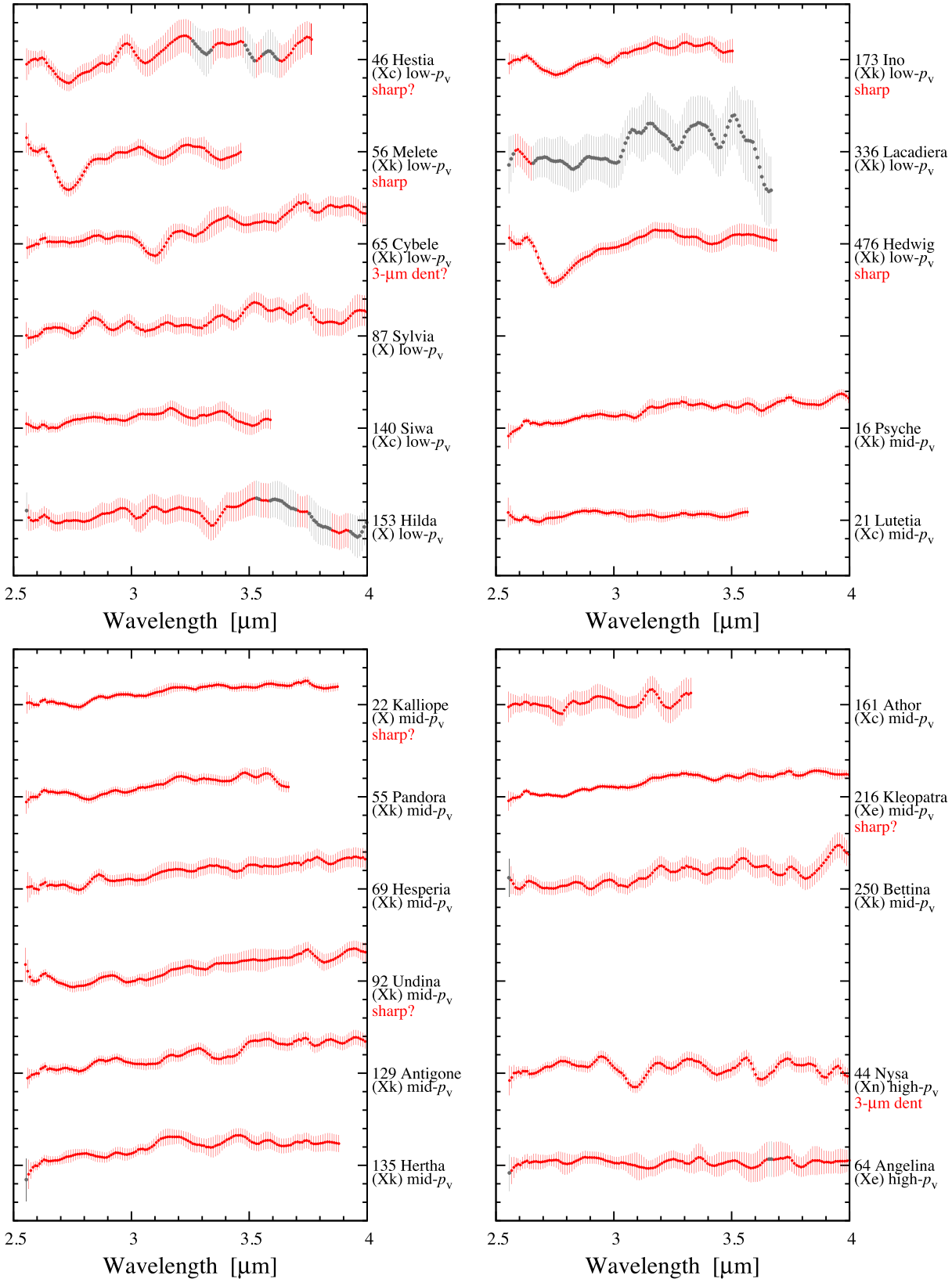

Fig. 6. Same as figure 5 but for X-complex asteroids. The objects are labeled by albedo value: low-p_v ($p_v < 0.1$), mid-p_v ($0.1 < p_v < 0.3$), and high-p_v ($p_v > 0.3$). (Color online)

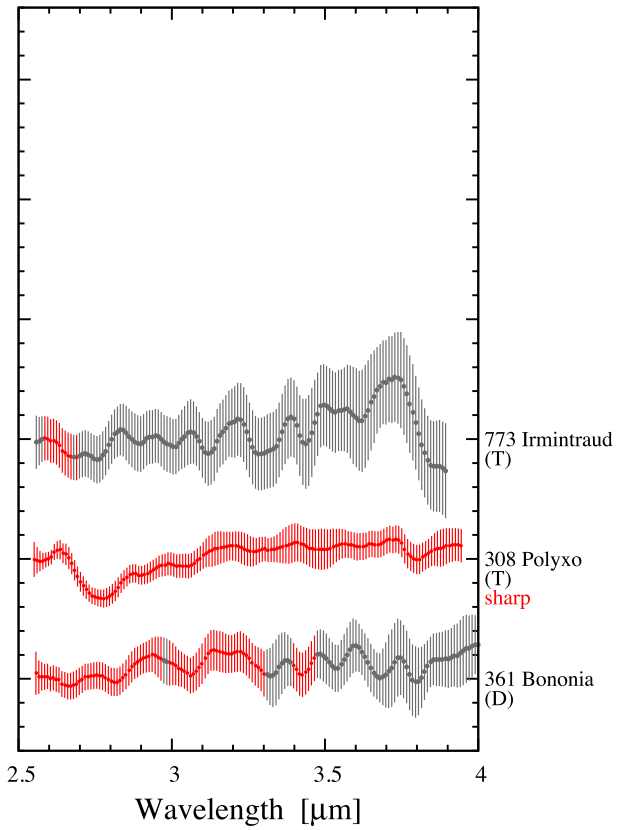

Fig. 7. Same as figure 5 but for D-complex asteroids. (Color online)

absorption objects (51 Nemausa: 47%, 13 Egeria: 41%, and 106 Dione: 36%), there is no clear correlation found. Figure 12 reveals the relationship in the 3.1 μm band, in which no clear correlation is observed.

Figures 13 and 14 show the distribution of peak absorption wavelengths for the 2.7 and 3.1 μm bands, respectively. The mean value of peak wavelength in the 2.7 μm band of 27 objects with $S/N > 2$ is 2.75 ± 0.03 μm, and that in the 3.1 μm band of 12 objects is 3.08 ± 0.02 μm. The uncertainty of the peak wavelength is estimated by a 1-pixel resolution of approximately 0.01 μm.

Figure 15 shows the relationship with the size of objects. Based on the size information from Usui et al. (2011), the largest 12 objects are analysed in this study, except for the following two objects: 31 Euphrosyne (276 km; Cb-type, Bus & Binzel 2002) and 15 Eunomia (256 km; K-type, DeMeo et al. 2009). Takir and Emery (2012) reported that 31 Euphrosyne is classified as Europa-like with a 13.63% band depth in the 3.00 μm band. These largest objects, with a diameter >250 km, have a band depth in the 2.7 μm band of moderate to weak ($10\% < \mathcal{D}_{2.7} < 30\%$), while some 150–250 km objects have greater band depths ($\mathcal{D}_{2.7} > 30\%$). On the other hand, no clear trend is observed in the distribution of the 3.1 μm band in figure 16.

Figures 17 and 18 show the relationship with the semi-major axis of objects. There are no clear trends in this distribution because the scatter is too large and the data suffered from significant observational bias.

Figure 19 displays the spectral slope measured in the 3 μm band. In this study, the spectral slope ($\mathcal{S}$) is defined as the slope from 2.6 μm to $\lambda_{\rm trunc}$ described in sub-subsection 2.2.4. The mean value of the slope of the asteroids which have an absorption feature in the 2.7 μm band ($\mathcal{D}_{2.7} > 10\%$) is $\overline{\mathcal{S}} = 0.004 \pm 0.033$, which is almost flat. In contrast, that of the asteroids which do not have a feature ($\mathcal{D}_{2.7} < 10\%$) is a positive slope ($\overline{\mathcal{S}} = 0.058 \pm 0.044$), which is likely to be connected with the slope of vis-NIR spectra.

3.2 Individual objects

Brief descriptions of 64 individual asteroids are given in this section.

3.2.1 C-complex asteroids

Most C-complex asteroids (17 out of 22), especially all Ch-, Cgh-, B-, and Cb-type asteroids, have obvious absorption features (>18%) at around 2.75 μm. Among C-complex asteroids, four types of spectral feature are observed: sharp, w-shape, 3 μm dent, and no clear significant feature. Moreover, in the sharp group, two subgroups exist: spectra with relatively large band depth ($\gtrsim$24%), whose features extend toward 3 μm or longer wavelengths, and spectra with moderate band depth ($\lesssim$24%), whose features end at around $\sim$2.9 μm. The former group either does not exhibit the 3.1 μm band feature or it is obscured by the strong 2.7 μm band feature. The latter may have other features longer than 3 μm (weak 3 μm dent). The former comprises Ch- and Cgh-types, while the latter belongs to other C-complex asteroids.

- C-type asteroids

  1 Ceres

  Ceres, classified as a dwarf planet, is the largest object in the main-belt region. This object is classified as a C-type asteroid and was the first object observed in the 3 μm band; i.e., Lebofsky (1978) clearly detected the 3 μm depth on its spectrum, King et al. (1992) discussed the existence of ammoniated phyllosilicate on Ceres, and Takir et al. (2015b) discussed phase angle-induced spectral effects on the 3 μm absorption band. Recently, Ceres has been comprehensively studied using in-situ observations of the spacecraft Dawn (Russell et al. 2004; Russell & Raymond 2011); an absorption band centered near 3.1 μm has been attributed to ammoniated phyllosilicates widespread across its surface (de Sanctis et al. 2015).

  The characteristics of the spectrum taken with AKARI are essentially consistent with those of

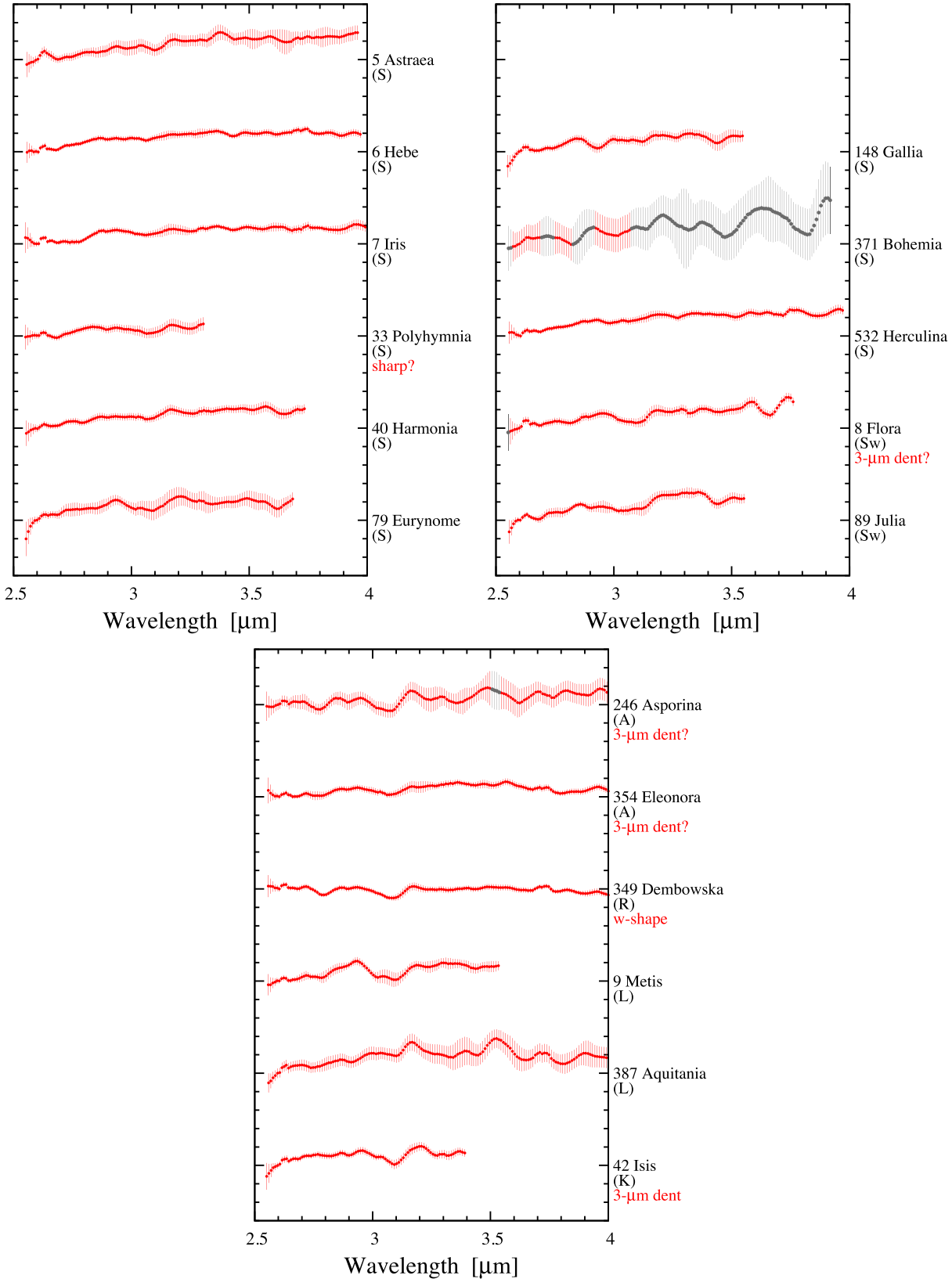

Fig. 8. Same as figure 5 but for S-complex asteroids. (Color online)

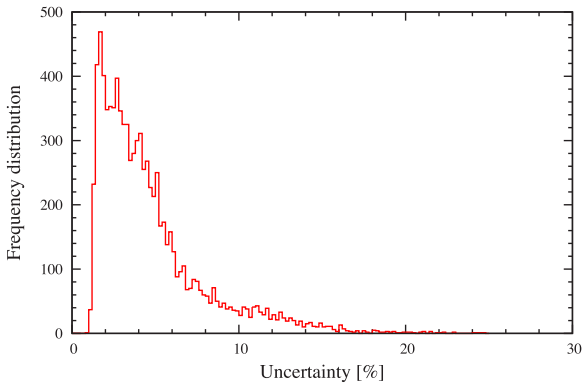

Fig. 9. Distribution of the uncertainties in the data points of all the reflectance spectra of 64 asteroids. The spectra within $<\lambda_{\rm trunc}$ are used for this histogram. (Color online)

previous research: the band centers located at 2.73 μm (2.72 μm, de Sanctis et al. 2015) and 3.08 μm (3.06–3.07 μm, Takir et al. 2015b). In this study, this spectral feature is categorized as w-shape. There is a bumpy structure at around 3.2 μm of uncertain origin, which is the similar feature found in Takir et al. (2015b) observed at the same phase angle of $\alpha \sim 22^\circ$.

10 Hygiea

Hygiea is a C-type asteroid, the fourth largest object (diameter of 430 km) in the main-belt region and is the largest member of its own family (Carruba 2013). Hygiea is a slow rotator, with one revolution lasting 27.63 hr (Warner et al. 2009). Hygiea has a fairly homogeneous surface (Mothé-Diniz et al. 2001). Takir and Emery (2012) classified the 3 μm band spectral feature of this object into the Ceres-like group. Our AKARI results also show that this object has two significant features at 2.72 and 3.08 μm; thus, this spectral feature is also categorized as w-shape.

24 Themis

Themis is a C-type asteroid. It is the largest member of its own family (e.g., D. Nesvorny 2015[5]). Fornasier et al. (1999) reported that this object has a signature of aqueous alteration based on ground-based observations at visible wavelengths. Takir and Emery (2012) classified the 3 μm band spectral feature of this object into the rounded group. The rounded shape has been previously identified by Campins et al. (2010). Rivkin and Emery (2010) found that the spectrum of Themis is matched by a spectral model of a mixture of ice-coated pyroxene grains and amorphous carbon, suggesting that the surfaces of these asteroids with rounded features include very fine water frost in the form of grain coatings. Our AKARI results show that its spectrum has two absorption features: at around 2.76 μm, which is associated with hydrated minerals, and at around 3.07 μm, a wide feature related to water ice; thus, this spectral feature is categorized as w-shape. The 3.1 μm feature of this object, which is thought to be associated with water ice, is broader than that of 1 Ceres or 10 Hygiea.

52 Europa

Europa is one of the largest C-type asteroids (diameter of 350 km). This object has a detailed 3-D shape model based on Adaptive Optics (AO) imaging observations made with the Keck telescope (Merline et al. 2013). D. Nesvorny (2015)[5] reported that this belongs to the Hygiea family. Takir and Emery (2012) classified the 3 μm band spectral feature of this object into the Europa-like group using its own name. Our results show a small 3.1 μm feature as well as a weaker feature at 2.7 μm, which is below the detection limit ($S/N < 2$).

81 Terpsichore

Terpsichore is a C-type asteroid and the largest member of the asteroid family bearing its name (D. Nesvorny 2015[5]). The albedo is 0.048 according to AKARI (Usui et al. 2011) or 0.034 according to WISE (Masiero et al. 2012), which is relatively dark among C-complex asteroids. There are no reports to-date of observations in the 3 μm band. Our AKARI results show the 2.7 μm feature, which is classified into the sharp group.

94 Aurora

Follow-up observations at 1–2.5 μm were performed by Hasegawa et al. (2017), and Aurora was classified as C-type according to the Bus–DeMeo taxonomy. No features have been observed yet in the 3 μm band; our results also show no significant feature in the 3 μm band.

128 Nemesis

Nemesis is a C-type asteroid and the largest member of the asteroid family bearing its name (D. Nesvorny 2015[5]). Nemesis is a slow rotator, taking 77.81 hr for one revolution (Warner et al. 2009). Heterogeneous surface properties were reported for this object by Scaltriti, Zappala, and Schober (1979). Our AKARI results show a significant feature in 2.74 μm, which is classified into the sharp group.

185 Eunike

Eunike is a C-type asteroid and a slow rotator, taking 21.812 hr for one revolution (Warner et al. 2009). Albedo variegation of this object was

[5] Nesvorny, D. 2015, NASA Planetary Data System, EAR-A-VARGBDET-5-NESVORNYFAM-V3.0.

Table 5. Band depth and peak wavelength in 2.7 μm and 3.1 μm.*

Object	Tax†	2.7 μm band depth		3.1 μm band depth		$\mathcal{S}$‡ [μm^{-1}]	3 μm band shape§
		$\mathcal{D}_{2.7}$[%]	λ_{peak}[μm]	$\mathcal{D}_{3.1}$[%]	λ_{peak}[μm]		
1 Ceres	C	**13.8 ± 1.2**	2.73 ± 0.01	**11.5 ± 1.7**	3.08 ± 0.01	0.007 ± 0.035	W-shape (Ceres-like)
2 Pallas	B	**29.3 ± 1.3**	2.74 ± 0.01	0.0 ± 1.9	3.09 ± 0.01	− 0.016 ± 0.030	Sharp
5 Astraea	S	3.5 ± 1.9	2.69 ± 0.01	4.1 ± 3.2	3.10 ± 0.01	0.091 ± 0.044	
6 Hebe	S	1.6 ± 1.0	2.68 ± 0.01	1.7 ± 1.4	3.06 ± 0.01	0.059 ± 0.028	
7 Iris	S	0.5 ± 1.0	2.68 ± 0.01	2.7 ± 1.6	3.06 ± 0.01	0.051 ± 0.031	
8 Flora	Sw	0.8 ± 1.6	2.69 ± 0.01	**5.6 ± 2.4**	3.09 ± 0.01	0.102 ± 0.037	3 μm dent?
9 Metis	L	1.3 ± 1.4	2.65 ± 0.01	7.8 ± 4.0	3.09 ± 0.01	0.080 ± 0.027	
10 Hygiea	C	**17.8 ± 1.6**	2.72 ± 0.01	**5.9 ± 2.1**	3.08 ± 0.01	0.053 ± 0.043	W-shape? (Ceres-like)
13 Egeria	Ch	**40.5 ± 1.6**	2.76 ± 0.01	2.9 ± 2.1	3.07 ± 0.01	0.013 ± 0.039	Sharp (sharp)
16 Psyche	Xk	0.9 ± 1.8	2.69 ± 0.01	4.2 ± 2.6	3.10 ± 0.01	0.106 ± 0.037	
21 Lutetia	Xc	2.4 ± 2.3	2.68 ± 0.01	1.2 ± 3.4	3.06 ± 0.01	0.032 ± 0.031	
22 Kalliope	X	**4.3 ± 1.9**	2.78 ± 0.01	2.3 ± 1.8	3.06 ± 0.01	0.068 ± 0.029	Sharp?
24 Themis	C	**10.4 ± 3.2**	2.76 ± 0.01	**11.9 ± 4.7**	3.07 ± 0.01	0.028 ± 0.057	W-shape? (Rounded)
33 Polyhymnia	S	**3.3 ± 1.5**	2.68 ± 0.01	2.4 ± 2.8	3.09 ± 0.01	0.075 ± 0.042	Sharp?
40 Harmonia	S	1.3 ± 1.5	2.69 ± 0.01	2.1 ± 2.0	3.09 ± 0.01	0.087 ± 0.030	
42 Isis	K	0.7 ± 1.4	2.71 ± 0.01	**7.9 ± 2.6**	3.09 ± 0.01	0.055 ± 0.029	3 μm dent
44 Nysa	Xn	2.6 ± 2.5	2.66 ± 0.01	**13.5 ± 3.2**	3.08 ± 0.01	− 0.017 ± 0.055	3 μm dent
46 Hestia	Xc	**12.3 ± 4.4**	2.73 ± 0.01	10.4 ± 7.2	3.06 ± 0.01	0.092 ± 0.087	Sharp?
49 Pales	Ch	**29.9 ± 3.1**	2.75 ± 0.01	0.3 ± 4.7	3.26 ± 0.01	0.003 ± 0.064	Sharp
50 Virginia	Ch	**23.9 ± 4.6**	2.74 ± 0.01	0.3 ± 5.1	3.06 ± 0.01	0.048 ± 0.100	Sharp
51 Nemausa	Cgh	**46.6 ± 2.9**	2.77 ± 0.01	6.4 ± 3.3	2.96 ± 0.01	− 0.023 ± 0.069	Sharp
52 Europa	C	5.5 ± 3.2	2.74 ± 0.01	**6.0 ± 2.5**	3.11 ± 0.01	− 0.022 ± 0.041	3 μm dent? (Europa-like)
55 Pandora	Xk	4.5 ± 2.3	2.82 ± 0.01	1.6 ± 2.4	2.98 ± 0.01	0.038 ± 0.036	
56 Melete	Xk	**20.0 ± 3.8**	2.73 ± 0.01	6.3 ± 4.2	3.14 ± 0.01	− 0.011 ± 0.059	Sharp
64 Angelina	Xe	0.3 ± 2.9	2.73 ± 0.01	5.1 ± 4.2	3.15 ± 0.01	0.011 ± 0.064	
65 Cybele	Xk	0.7 ± 2.8	2.74 ± 0.01	**11.3 ± 4.5**	3.10 ± 0.01	0.108 ± 0.062	3 μm dent? (Rounded)
69 Hesperia	Xk	5.6 ± 2.8	2.79 ± 0.01	1.9 ± 3.3	3.05 ± 0.01	0.108 ± 0.056	
79 Eurynome	S	1.0 ± 3.3	2.72 ± 0.01	6.1 ± 5.2	3.09 ± 0.01	0.098 ± 0.043	
81 Terpsichore	C	**15.0 ± 4.6**	2.73 ± 0.01	2.9 ± 5.9	3.08 ± 0.01	− 0.002 ± 0.109	Sharp
87 Sylvia	X	5.1 ± 3.3	2.76 ± 0.01	4.4 ± 3.6	3.06 ± 0.01	0.087 ± 0.079	
89 Julia	Sw	2.3 ± 1.9	2.68 ± 0.01	0.3 ± 2.5	3.06 ± 0.01	0.112 ± 0.029	
92 Undina	Xk	**6.0 ± 2.9**	2.76 ± 0.01	4.4 ± 3.6	3.06 ± 0.01	0.096 ± 0.057	Sharp?
94 Aurora	C	3.8 ± 2.9	2.74 ± 0.01	2.9 ± 3.2	3.07 ± 0.01	− 0.020 ± 0.069	
106 Dione	Cgh	**36.0 ± 3.4**	2.76 ± 0.01	4.9 ± 4.0	3.08 ± 0.01	0.035 ± 0.073	Sharp
121 Hermione	Ch	**24.8 ± 2.5**	2.78 ± 0.01	3.7 ± 2.9	3.06 ± 0.01	− 0.002 ± 0.060	Sharp (sharp)
127 Johanna	Ch	**23.2 ± 8.5**	2.81 ± 0.01	3.7 ± 11.0	2.98 ± 0.01	0.009 ± 0.138	Sharp?
128 Nemesis	C	**19.1 ± 2.2**	2.74 ± 0.01	3.4 ± 2.7	3.06 ± 0.01	− 0.068 ± 0.055	Sharp
129 Antigone	Xk	3.9 ± 2.2	2.79 ± 0.01	4.8 ± 3.2	3.10 ± 0.01	0.112 ± 0.044	
135 Hertha	Xk	1.0 ± 2.3	2.69 ± 0.01	2.7 ± 3.1	3.07 ± 0.01	0.086 ± 0.049	
140 Siwa	Xc	0.6 ± 2.9	2.72 ± 0.01	1.8 ± 3.3	2.97 ± 0.01	0.037 ± 0.056	(Featureless)
145 Adeona	Ch	**28.9 ± 6.0**	2.76 ± 0.01	12.8 ± 11.1	3.12 ± 0.01	0.082 ± 0.116	Sharp
148 Gallia	S	1.2 ± 1.8	2.75 ± 0.01	2.6 ± 2.6	3.12 ± 0.01	0.073 ± 0.033	
153 Hilda	X	2.7 ± 4.5	2.68 ± 0.01	5.4 ± 7.2	3.02 ± 0.01	− 0.017 ± 0.114	(Rounded)
161 Athor	Xc	6.3 ± 6.5	2.78 ± 0.01	7.8 ± 6.2	3.09 ± 0.01	0.078 ± 0.093	
173 Ino	Xk	**9.1 ± 2.2**	2.75 ± 0.01	3.9 ± 2.8	2.97 ± 0.01	0.043 ± 0.070	Sharp
185 Eunike	C	5.5 ± 5.0	2.69 ± 0.01	13.6 ± 7.6	3.06 ± 0.01	0.007 ± 0.117	
216 Kleopatra	Xe	**3.3 ± 1.3**	2.78 ± 0.01	2.6 ± 1.9	3.07 ± 0.01	0.078 ± 0.028	Sharp?
246 Asporina	A	5.3 ± 3.0	2.78 ± 0.01	**8.7 ± 3.7**	3.08 ± 0.01	0.037 ± 0.065	3 μm dent?
250 Bettina	Xk	3.5 ± 3.6	2.74 ± 0.01	5.7 ± 4.3	3.06 ± 0.01	0.129 ± 0.070	
308 Polyxo	T	**14.6 ± 3.5**	2.76 ± 0.01	3.2 ± 5.1	3.06 ± 0.01	0.023 ± 0.075	Sharp (sharp)
336 Lacadiera	Xk	5.2 ± 9.2	2.65 ± 0.01	6.5 ± 12.9	3.02 ± 0.01	− 0.180 ± 0.230	
349 Dembowska	R	**3.8 ± 1.2**	2.79 ± 0.01	**6.0 ± 1.6**	3.09 ± 0.01	− 0.033 ± 0.023	W-shape

Table 5. (Continued)

Object	Tax†	2.7 μm band depth		3.1 μm band depth		$\mathcal{S}^{\ddagger}$ [μm^{-1}]	3 μm band shape§
		$\mathcal{D}_{2.7}$[%]	λ_{peak}[μm]	$\mathcal{D}_{3.1}$[%]	λ_{peak}[μm]		
354 Eleonora	A	1.0 ± 1.7	2.72 ± 0.01	**4.0 ± 1.5**	3.06 ± 0.01	0.016 ± 0.026	3 μm dent?
361 Bononia	D	3.5 ± 5.6	2.67 ± 0.01	8.8 ± 7.4	3.06 ± 0.01	0.098 ± 0.117	(rounded)
371 Bohemia	S	6.8 ± 9.9	2.83 ± 0.01	4.1 ± 9.0	3.02 ± 0.01	0.169 ± 0.159	
387 Aquitania	L	1.9 ± 2.8	2.76 ± 0.01	4.3 ± 3.7	3.10 ± 0.01	0.042 ± 0.063	
419 Aurelia	C	12.6 ± 7.9	2.80 ± 0.01	6.1 ± 9.7	3.12 ± 0.01	− 0.067 ± 0.194	
423 Diotima	C	**5.9 ± 2.6**	2.79 ± 0.01	4.9 ± 3.2	3.02 ± 0.01	− 0.025 ± 0.062	Sharp?
451 Patientia	C	9.8 ± 6.1	2.78 ± 0.01	**9.6 ± 4.5**	3.06 ± 0.01	0.061 ± 0.100	3 μm dent? (Europa-like)
476 Hedwig	Xk	**23.5 ± 2.9**	2.75 ± 0.01	1.2 ± 3.8	3.06 ± 0.01	0.003 ± 0.070	Sharp
511 Davida	C	**22.5 ± 1.8**	2.73 ± 0.01	4.3 ± 2.9	3.09 ± 0.01	− 0.034 ± 0.064	Sharp (sharp)
532 Herculina	S	0.9 ± 1.1	2.69 ± 0.01	2.0 ± 1.7	2.98 ± 0.01	0.092 ± 0.027	
704 Interamnia	Cb	**18.2 ± 1.5**	2.74 ± 0.01	2.2 ± 2.4	3.12 ± 0.01	0.000 ± 0.041	Sharp (sharp)
773 Irmintraud	T	10.3 ± 9.9	2.76 ± 0.01	11.1 ± 13.4	3.12 ± 0.01	− 0.097 ± 0.251	

*The values with $S/N > 2$ (treated as significant features in this work) is shown in bold face.
†Bus–DeMeo taxonomy (see table 2).
‡Spectral slope in the 3 μm band.
§The 3 μm band shape determined by combination of $\mathcal{D}_{2.7}$ and $\mathcal{D}_{3.0}$ (see text). Takir classification (see table 2) is given in parentheses.

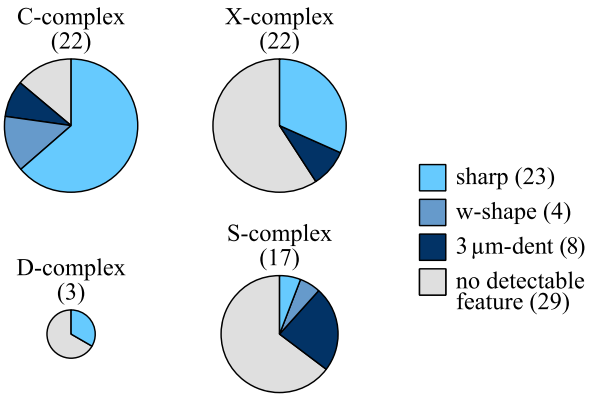

Fig. 10. Numbers of the 3 μm band shapes classified in this study. (Color online)

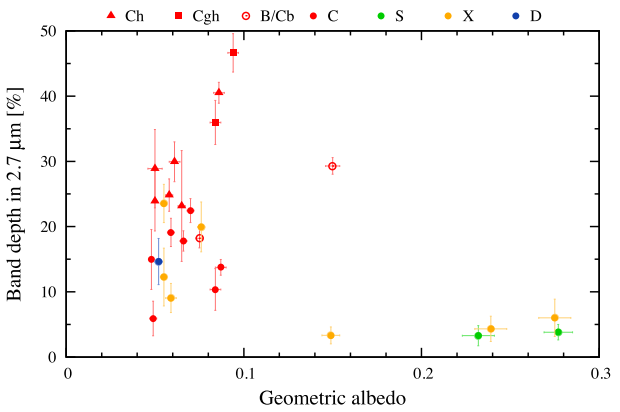

Fig. 11. Distribution of band depths in the 2.7 μm band of reflectance spectra ($S/N > 2$) against geometric albedo. The red, green, yellow, and blue symbols denote C-, S-, X-, and D-complex asteroids, respectively. C-complex asteroids are subdivided into rectangles, triangles, open circles, and filled circles, as Cgh-, Ch-, B, or Cb, and other C-type, respectively. The correlation coefficient is −0.46. (Color online)

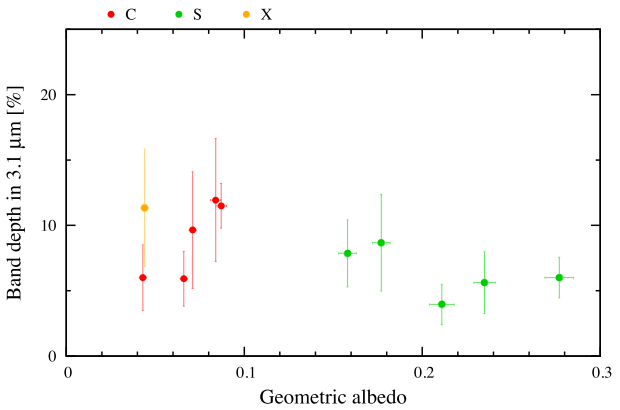

Fig. 12. Same as figure 11 but in the 3.1 μm band. The correlation coefficient is 0.11. (Color online)

reported by Pilcher et al. (2014). Fornasier et al. (1999) reported that this object does not exhibit an aqueous alteration signature according to ground-based observations at visible wavelengths. Rivkin et al. (2003) reported an absorption feature of 5.3% towards 2.7 μm, but our results show no feature in the 3 μm band. Note that the signal of this object observed with AKARI was faint (∼9 mJy in 3 μm, or the apparent visual magnitude of APmag = 13.35) and no significant spectral feature was observed above the detection limit.

419 Aurelia

Aurelia is a C-type asteroid (or F-type in the Tholen taxonomy). The signal observed by AKARI was faint (∼6 mJy in 3 μm, or APmag = 13.73). It has an absorption feature at around 2.8 μm, but it was too noisy and below the detection limit.

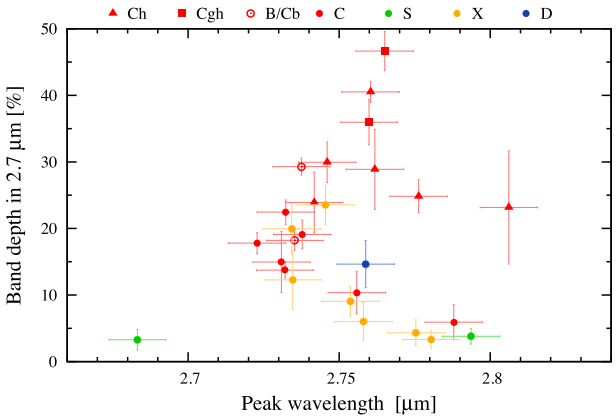

Fig. 13. Same as figure 11 but against the peak wavelength of band depth in the 2.7 μm band. The correlation coefficient is 0.02. (Color online)

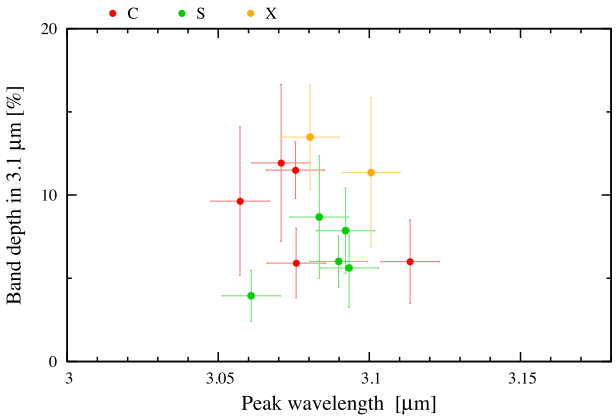

Fig. 14. Same as figure 13 but in the 3.1 μm band. The correlation coefficient is −0.12. (Color online)

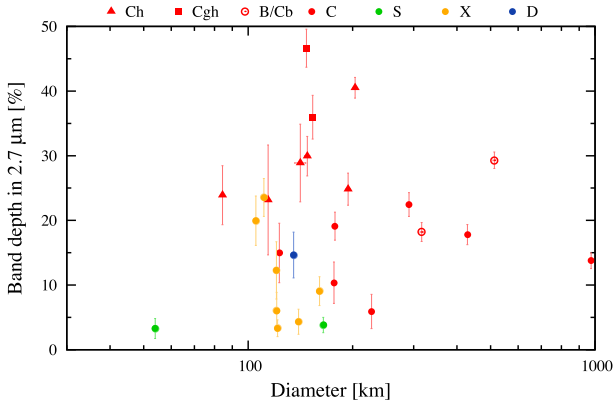

Fig. 15. Same as figure 11 in the 2.7 μm band but against the asteroid diameter. The correlation coefficient is 0.03. (Color online)

423 Diotima

Follow-up observations in 1–2.5 μm were performed by Hasegawa et al. (2017), and Diotima was classified as C-type according to the Bus–DeMeo taxonomy. This object is a member

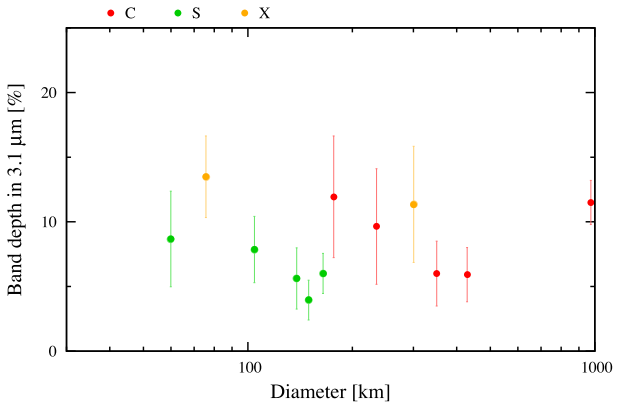

Fig. 16. Same as figure 15 but in the 3.1 μm band. The correlation coefficient is 0.18. (Color online)

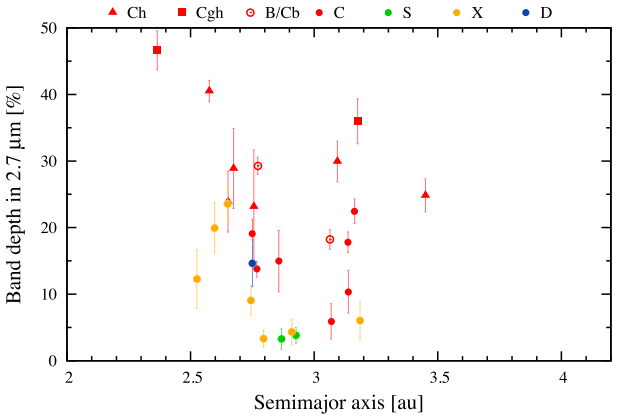

Fig. 17. Same as figure 11 in the 2.7 μm band but against the semimajor axis of asteroids. The correlation coefficient is −0.25. (Color online)

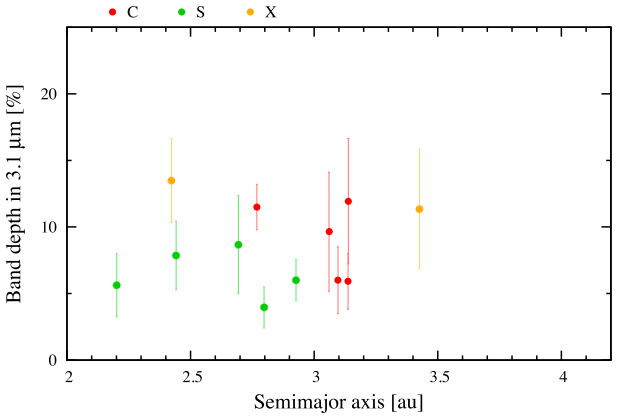

Fig. 18. Same as figure 17 but in the 3.1 μm band. The correlation coefficient is 0.11. (Color online)

of the Eos collisional family (D. Nesvorny 2012,[6] not in D. Nesvorny 2015[5]), but is likely to be an interloper based on a spin-state analysis (Hanuš et al. 2018). Jones et al. (1990) conducted 3 μm

[6] Nesvorny, D. 2012, NASA Planetary Data System, EAR-A-VARGBDET-5-NESVORNYFAM-V2.0

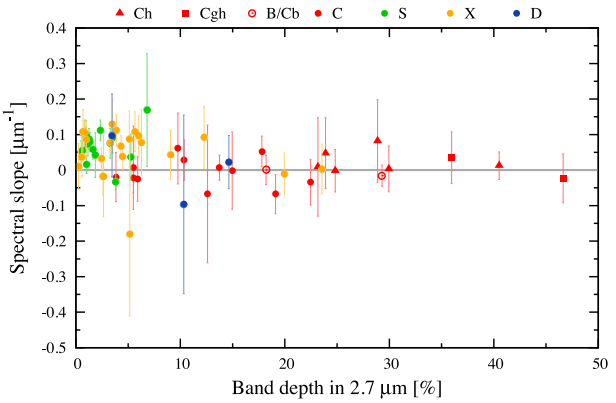

Fig. 19. Distribution of the spectral slope measured from 2.6 μm to $\lambda_{\rm trunc}$ in the reflectance spectra against the band depth in the 2.7 μm band. The solid gray line indicates a horizontal line of zero slope ($\mathcal{S} = 0$). To clarify the plot, the error bars of band depth (in the horizontal direction) are omitted. The correlation coefficient is −0.33. (Color online)

band observations with IRTF and detected no signal associated with hydrated minerals and/or water ice. Our AKARI results show an absorption feature at around 2.79 μm, but its spectral shape is shallower and wider than that of typical hydrated minerals found in other asteroids in this study.

451 Patientia

Patientia is a C-type asteroid, or Cb-type in the Bus taxonomy (Lazzaro et al. 2004), and it has a very flat light curve, indicating a spherical body (Michałowski et al. 2005). Takir and Emery (2012) classified the 3 μm band spectral feature of this object into the Europa-like group. Our AKARI results show absorption features at around 3.06 μm, which are classified as the 3 μm dent. A spectral feature appears at around 2.78 μm, but is below the detection limit.

511 Davida

This object is a C-type asteroid and a member of the Meliboea family (D. Nesvorny 2015[5]). A shape model of this object was given by Conrad et al. (2007) based on Keck AO observations, and its volume and bulk density are discussed by Viikinkoski et al. (2017). Its bulk density ($2.1 \pm 0.4\,{\rm g\,cm^{-3}}$) suggests some degree of differentiation within the interior of the object. Takir and Emery (2012) classified the 3 μm band spectral feature of this object into the sharp group. Our AKARI results show absorption features at around 2.73 μm and, to a lesser degree, the 3.1 μm feature, which is below the detection limit. Its spectral shape is classified into the sharp group.

- B- and Cb-type asteroids

2 Pallas

Pallas is a B-type asteroid and the third largest asteroid in the main-belt region; it is associated with a collisional family (Lemaitre & Morbidelli 1994) that resulted from a cratering event. It is reported that the albedo and spectral properties of the Pallas collisional family members differ from those of other B-types (Asensio Ramos & Arregui 2013; Alí-Lagoa et al. 2016). Schmidt and Castillo-Rogez (2012) discussed that water may play an important role in the thermal–physical evolution of this object. The surface heterogeneity of this object was detected with ground-based telescopes and Hubble observations (Schmidt et al. 2009; Carry et al. 2010). Our AKARI results show a significant feature found at around 2.74 μm, which appears to be similar to the sharp group in Takir and Emery (2012). Rivkin et al. (2015) discussed that the spectral shapes of Ch-type asteroids have the same spectral shape as that of 2 Pallas; i.e., "Pallas-type" spectral group, which is consistent with the presence of phyllosilicates. In the AKARI observations, it is sufficiently bright and (partly) saturates the observed signal on the detector as described in sub-subsection 2.2.2, while no unusual behavior is found in the spectra compared with the literature.

704 Interamnia

Interamnia is a Cb-type asteroid with a diameter of 320 km. It is one of the largest bodies in the main belt, but is not associated with a family (Rivkin et al. 2014). In the Tholen taxonomy, it is classified as F-type. Polarimetric observations suggest that this object has peculiar surface properties (Belskaya et al. 2005). Takir and Emery (2012) classified the 3 μm band spectral feature of this object into the sharp group. Our AKARI results also show absorption features at around 2.74 μm, which is classified as the sharp group.

- Cgh- and Ch-type asteroids

51 Nemausa

Nemausa is a Cgh-type asteroid (or Ch-type in the Bus taxonomy). Fornasier et al. (1999) reported that this object displays an aqueous alteration signature according to ground-based observations at visible wavelengths. Rivkin et al. (2015b) reported a strong absorption feature for this object in the 3 μm band. Our AKARI results also show a significant absorption feature at around 2.77 μm, which belongs to the sharp group. The band depth at 2.7 μm for this object is the strongest among all targets in this study (∼47%).

106 Dione

Dione is a Cgh-type asteroid, for which Rivkin et al. (2003) reported evidence of hydration in the 3 μm band with a ground-based telescope. Our AKARI results show a significant absorption

feature at around 2.76 μm, which is classified as the sharp group.

13 Egeria

Egeria is a Ch-type asteroid. Burbine (1998) discussed that the band shape at around 0.7 μm is associated with CM chondrites. Rivkin et al. (2003) reported evidence of hydration in the 3 μm band with a ground-based telescope. Takir, Emery, and McSween (2015a) classified the 3 μm band spectral feature of this object into the sharp group, which is confirmed by our AKARI results to be at around 2.76 μm.

49 Pales

Pales is a Ch-type asteroid and a slow rotator, taking 20.70 hr for one revolution (Warner et al. 2009). No studies to-date report observations in the 3 μm band; however, our AKARI results show an absorption feature at around 2.75 μm, which is classified into the sharp group.

50 Virginia

Virginia is a Ch-type asteroid, or X-type in the Tholen taxonomy. Virginia has no observations in the 3 μm band so far. Conversely, our AKARI results show an absorption feature at around 2.74 μm, which is classified into the sharp group; however, the signal observed with AKARI is faint ($\sim$9 mJy in 3 μm, or APmag = 13.21).

121 Hermione

Hermione is a Ch-type asteroid in the Cybele group. Hermione is a binary system with a moon S/2002 (121) 1 with a diameter of $\sim$12 km (Marchis et al. 2006), which converts to a diameter ratio for this system of 0.06. Takir and Emery (2012) classified the 3 μm band spectral feature of this object into the sharp group. Hargrove et al. (2012) found a deep 3 μm absorption feature with IRTF observations and no 10 μm emission feature with Spitzer/IRS. Our AKARI results also show an absorption feature at around 2.78 μm, which is classified into the sharp group. Two observations were performed with AKARI at 9.9 hr intervals; no significant difference is observed.

127 Johanna

Hasegawa et al. (2017) reported that Johanna is classified as Ch-type in the Bus–DeMeo taxonomy and Rivkin et al. (2015b) reported an absorption feature of it in the 3 μm band. The signal for this object observed with AKARI is faint ($\sim$5 mJy in 3 μm, or APmag = 13.91). One feature appears at around 2.81 μm, which is classified into the sharp group, but it is almost indiscernible from the noise.

145 Adeona

Adeona is a Ch-type asteroid and the largest member of the asteroid family bearing its name (D. Nesvorny 2015[5]). Fornasier et al. (1999) reported an aqueous alteration signature according to ground-based observations at visible wavelengths. The signal according to AKARI is faint ($\sim$9 mJy in 3 μm, or APmag = 13.03). One feature appears at around 2.76 μm, which is classified into the sharp group.

3.2.2 X-complex asteroids

We divide the X-complex into three groups according to their albedo (cf. Tholen 1984): low albedo ($p_v < 0.1$), moderate albedo ($0.1 < p_v < 0.3$), and high albedo ($p_v > 0.3$). Some low- and moderate-albedo X-complex asteroids have an absorption feature in the 2.7 μm band, similar to the C-complex asteroids.

- Low-albedo X-complex asteroids

46 Hestia

Hestia is an Xc-type asteroid (or P-type in the Tholen taxonomy). It is a slow rotator, with one revolution lasting 21.04 hr (Warner et al. 2009). There are no reports to-date of features in the 3 μm band. Fieber-Beyer and Gaffey (2015) discussed the relationship between the surface minerals of Hestia and CR chondrites based on the vis-NIR observations. Our AKARI results show absorption features at around 2.74 μm, which is classified as the sharp group, and some features at around 3.1 μm, but the spectral shape appears bumpy. The observed signal is faint ($\sim$12 mJy in 3 μm, or APmag = 13.42) and its spectrum suffered from noise. Two observations were performed with AKARI at 100 min intervals with no significant difference found between them.

56 Melete

Melete is an Xk-type asteroid (or P-type in the Tholen taxonomy). No features have yet been observed in the 3 μm band. Our AKARI results show absorption features at around 2.73 μm (sharp). There is also a small feature at around 3.1 μm, which is below the detection limit.

65 Cybele

Cybele, an Xk-type asteroid (or P-type in the Tholen taxonomy) with a diameter of 300 km, belongs to the Cybele group bearing its own name, which is located in the outer main-belt region. Licandro et al. (2011) made spectroscopic observations with IRTF and found an absorption band centered at 3.10 μm, which is associated with water ice as frost, but no feature associated with hydrated silicates in the 2–4 μm band. The former feature is similar to that

of C-type asteroid 24 Themis. Takir and Emery (2012) classified the 3 μm band spectral feature of this object into the rounded group. Our AKARI results also show an absorption feature at around 3.1 μm, but its spectral shape is sharper than previous works.

87 Sylvia

Sylvia is an X-type asteroid (or P-type in the Tholen taxonomy) and is a triple system with two moons, Remus and Romulus, with respective diameters of $\sim$7 km and $\sim$18 km (Marchis et al. 2005). The respective diameter ratios of this system are 0.03 and 0.07. There are no previous reports of spectroscopic observations in the 3 μm band. The signal of this object observed with AKARI is faint ($\sim$13 mJy in 3 μm, or APmag = 13.30); it shows some features in the 3 μm band, but they are below the detection limit.

140 Siwa

Siwa is an Xc-type asteroid (or P-type in the Tholen taxonomy) and a slow rotator, taking 34.45 hr for one revolution (Warner et al. 2009). No absorption features were found in previous studies (Takir & Emery 2012); i.e., it is a featureless object. Our AKARI results also show no significant features in the 3 μm band.

153 Hilda

Hilda is an X-type asteroid (or P-type in the Tholen taxonomy) and the largest member of the asteroid family bearing its name (D. Nesvorny 2015[5]). Takir and Emery (2012) classified the 3 μm band spectral feature of this object into the rounded group. The signal observed by AKARI is faint ($\sim$7 mJy in 3 μm, or APmag = 14.01); thus, we cannot identify any significant features with a sufficient S/N ratio.

173 Ino

Ino is an Xk-type asteroid and the largest member of the asteroid family bearing its name (D. Nesvorny 2015[5]). Jones et al. (1990) reported some hydration of this object. Our AKARI results show an absorption feature at around 2.75 μm, which is classified into the sharp group. A small dent shape of uncertain origin appears at around 2.97 μm.

336 Lacadiera

Lacadiera is an Xk-type asteroid (or D-type in the Tholen taxonomy). There are no previous reports of hydration detected in the 3 μm band (e.g., Cruikshank et al. 2002). The signal observed by AKARI is too faint ($\sim$4 mJy in 3 μm, or APmag = 14.24); thus, no significant features were observed with a sufficient S/N ratio.

476 Hedwig

Hedwig is an Xk-type asteroid (or P-type in the Tholen taxonomy) and is a slow rotator, with one revolution lasting 27.33 hr (Warner et al. 2009). No spectroscopic observations have been made in the 3 μm band. The AKARI signal is faint ($\sim$11 mJy in 3 μm, or APmag = 13.42); however, this object has a sharp spectral feature at around 2.75 μm, which is typically found in C-complex asteroids in AKARI data.

- Moderate-albedo X-complex asteroids

16 Psyche

Psyche is an Xk-type asteroid (or M-type in the Tholen taxonomy). The Psyche mission was selected by the NASA Discovery program to rendezvous with asteroid 16 Psyche (Elkins-Tanton et al. 2017). Radar albedo (Ostro et al. 1985; Magri et al. 2007; Shepard et al. 2008, 2017), thermal inertia (Matter et al. 2013), and density estimation (Kuzmanoski & Kovačević 2002) indicate that this asteroid has a predominantly metal-rich surface. There is no dynamical family associated with this object (Davis et al. 1999). Takir et al. (2017) detected a 3 μm band feature at a $\sim$3% level, possibly associated with water or hydroxyl, which is proposed to have exogenic origins (e.g., Landsman et al. 2018; Avdellidou et al. 2018). In contrast, our AKARI data indicate no significant absorption feature in the 3 μm band. Note that a $\sim$4% band depth at around 3.1 μm is found in our data, but it is below the detection limit. Two observations were performed with AKARI at 100 min intervals with no difference found between them.

21 Lutetia

Lutetia is an Xc-type asteroid (or M-type in the Tholen taxonomy). Its bulk density was determined from the spacecraft Rosetta flyby as 3.4 ± 0.3 g cm^{-3} (Pätzold et al. 2011). Rosetta also performed spectroscopy of Lutetia (Coradini et al. 2011) and reported no absorption features in the spectral range from 0.4 to 3.5 μm. IRTF observations (Vernazza et al. 2011) also revealed absence of 3 μm features. On the other hand, Rivkin et al. (2011) reported the detection of a 3 μm band feature at the 3%–5% level in the southern hemisphere, the other side of the asteroid which is not visible to Rosetta (Rivkin et al. 2015a; Barucci & Fulchignoni 2017). Our AKARI results show no absorption features in the 3 μm band. A small dent shape with a $\sim$2% band depth appears at around 2.7 μm, which might come from contamination due to background stars.

22 Kalliope

Kalliope is an X-type asteroid (or M-type in the Tholen taxonomy) with an albedo of 0.24 (Usui et al. 2011) and bulk density of 3.35 g cm^{-3} (Descamps et al. 2008). It is a binary system with a moon, Linus (22 Kalliope I), with a diameter of 28 km and an orbital period of 3.5954 d (Descamps et al. 2008). The diameter ratio of this system is 0.2. Rivkin et al. (2000) showed evidence for hydrated minerals on Kalliope with a ∼10% band depth in the 3 μm band based on IRTF observations. Our AKARI results show a small feature with a ∼4% band depth at around 2.78 μm. Two observations were performed with AKARI at 3.3 hr intervals with no significant difference.

55 Pandora

Pandora is an Xk-type asteroid (or M-type in the Tholen taxonomy) with a relatively high albedo: 0.34 observed by AKARI (Usui et al. 2011) or 0.20 according to WISE (Masiero et al. 2012). Jones et al. (1990) reported an absorption feature in the 3 μm band, and Rivkin et al. (2000) also showed a hydration feature with a band depth of ∼9% and temporal variation in this spectral feature. Our AKARI results show a feature at around 2.8 μm, which is below the detection limit. Three observations were performed with AKARI within 6.6 hr but all of them suffered from contamination due to background stars.

69 Hesperia

Hesperia is an Xk-type asteroid (or M-type in the Tholen taxonomy). Landsman et al. (2015) reported a 3 μm absorption feature with a band depth of 6.2%. Our AKARI results show a feature at around 2.8 μm that is below the detection limit. Note that only one pointed observation was conducted for this object with AKARI.

92 Undina

Undina is an Xk-type asteroid. Rivkin et al. (2000) reported a 3 μm absorption feature with a band depth of 9.3%. Our AKARI results show a small feature with a ∼6% band depth at around 2.76 μm.

129 Antigone

Antigone is an Xk-type asteroid (or M-type in the Tholen taxonomy). Rivkin et al. (2000) reported a 3 μm absorption feature with a band depth of 14.4%. Our AKARI results show a peculiar wavy structure related to contamination by background stars (the magnitude in the K band of Kmag = 13.5 in the data of Obs ID:1520147-001, and Kmag = 15.7 in the data of Obs ID:1520148-001).

135 Hertha

Hertha is an Xk-type asteroid (or M-type in the Tholen taxonomy) and is one of the largest members in the Nysa–Polana complex (e.g., Dykhuis & Greenberg 2015). Rivkin et al. (2000) reported a 3 μm absorption feature with a band depth of 10.2% and Rivkin et al. (2002) discussed the 0.7 μm absorption of this object. Our AKARI results show a peculiar wavy structure of uncertain origin, which is below the detection limit.

161 Athor

Athor is an Xc-type asteroid (or M-type in the Tholen taxonomy). Rivkin et al. (2000) reported an absence of 3 μm features. The signal observed with AKARI is too faint (∼12 mJy in 3 μm, or APmag = 13.31) to identify any significant feature with a sufficient S/N ratio.

216 Kleopatra

Kleopatra is an Xe-type asteroid (or M-type in the Tholen taxonomy), which is famous for its peculiar bilobate, or "dog-bone" shape (Ostro et al. 2000). This is a triple system with two moons, Cleoselene and Alexhelios, with diameters of ∼7 km and ∼9 km, respectively (Descamps et al. 2011). Diameter ratios of this system are 0.06 and 0.07. Landsman et al. (2015) showed evidence for hydrated minerals in Kleopatra using IRTF observations; approximately 5% on average, as well as rotational variability in the depth of its 3 μm feature. Our AKARI results show a small feature with a ∼3% band depth at around 2.78 μm. Three observations were performed with AKARI; the first two were separated by 5 hr intervals and the last was conducted 1.46 yr after the first two because of observational scheduling. Among these three, no significant spectral differences are observed above the noise level.

250 Bettina

Bettina is an Xk-type asteroid (or M-type in the Tholen taxonomy). Vernazza et al. (2009) discussed a similarity of spectral shape between this object and mesosiderite, a stony-iron meteorite, at 0.4–2.5 μm. No observations exist in the 3 μm band. The signal observed by AKARI is faint (∼13 mJy in 3 μm, or APmag = 13.31) and no significant absorption feature is found in the 3 μm band. One data (Obs ID:1520161-001) is removed by contamination so only one observational data is used for this object.

- High-albedo X-complex asteroids

44 Nysa

Nysa is an Xn-type asteroid (or E-type in the Tholen taxonomy) with a high albedo of 0.48 (Usui et al. 2011; Masiero et al. 2012). Owing to its high albedo, the contribution of thermal emission is small at 2.5–5 μm. It is the largest member of the

Nysa-Polana family (D. Nesvorny 2015[5]). Rivkin et al. (1995) detected the 3 μm band depth on Nysa with 14%, which is attributed to hydrated minerals. By removing one data (Obs ID:1520189-001) due to contamination as described above, only one observational data from AKARI is used for this object. It shows a peculiar wavy structure of uncertain origin. An unidentified feature is also observed with a ~14% band depth at around 3.08 μm.

64 Angelina

Angelina is an Xe-type asteroid (or E-type in the Tholen taxonomy) with a high albedo; 0.52 according to AKARI (Usui et al. 2011) or 0.48 for WISE (Masiero et al. 2014). Owing to its high albedo, the thermal emission contribution is small at 2.5–5 μm. There are no reports of observations in the 3 μm band. The signal observed by AKARI is faint (~12–13 mJy in 3 μm, or APmag = 12.83) and its spectrum is flat with no features in the 3 μm band.

3.2.3 D-complex asteroids

D-complex asteroids are darker and located further from the observer; thus, these asteroids are fainter (APmag > 13). One has an absorption feature in the 2.7 μm band, like C-complex asteroids, and the other two do not.

773 Irmintraud

Irmintraud is a T-type asteroid, and there are a couple of reports suggesting the existence of water on this object (e.g., Lebofsky et al. 1990; Jones et al. 1990; Howell 1995; Merényi et al. 1997). Kanno et al. (2003) performed near-infrared photometric and spectroscopic observations of this object and concluded that the Tagish Lake meteorite is related to D-type asteroids. The signal observed by AKARI is faint (~5 mJy in 3 μm, or APmag = 14.36) and the data quality is not sufficient to interpret any pattern in the spectral shape at 2.5–3.5 μm, which is almost hidden by noise; thus, no significant features are identified with a sufficient S/N ratio.

308 Polyxo

Polyxo is a T-type asteroid. Rivkin et al. (2002) reported that most T-types have a 3 μm band feature. Hiroi and Hasegawa (2003) made spectral fitting between Polyxo with ground-based observations and the Tagish Lake meteorite. Takir and Emery (2012) classified the 3 μm band spectral feature of this object into the sharp group. The AKARI signal for this object is faint (~13 mJy in 3 μm, or APmag = 13.34); however, it has a sharp spectral feature with a ~15% band depth at around 2.76 μm, which is typically found in C-complex asteroids in AKARI data.

361 Bononia

Bononia is a D-type asteroid and belongs to the Hilda group. Takir and Emery (2012) classified the 3 μm band spectral feature of this object into the rounded group. The AKARI signal of this object is faint (~6 mJy in 3 μm, or APmag = 14.26). A pattern is observed in the spectral shape at 2.5–3.5 μm, which is almost indistinguishable from noise; thus, no significant features have a sufficient S/N ratio.

3.2.4 S-complex asteroids

Our AKARI results show that only a few S-complex asteroids have an absorption feature with a few percent band depth in the 3 μm band.

5 Astraea

Astraea is an S-type asteroid. Jones et al. (1990) observed Astraea with IRTF and reported no absorption feature in the 3 μm band. Our AKARI results also show no significant feature in the spectrum of this object.

6 Hebe

Hebe is an S-type asteroid. Rivkin et al. (2001) detected a 3%–5% band depth in the 3 μm band of this object with UKIRT. This level of feature is below the detection limit of AKARI observations, and our results indicate no significant feature in this object.

7 Iris

Iris is an S-type asteroid. Rivkin (1997) did not detect any hydrated minerals on this object with IRTF. Our AKARI results also show no significant feature in the spectrum of this object in the 3 μm band.

33 Polyhymnia

Polyhymnia is an S-type asteroid. No previous observations have been reported for the 3 μm band. Our AKARI results show a small feature with a ~3% band depth at around 2.68 μm.

40 Harmonia

Harmonia is an S-type asteroid, and our AKARI results show no significant feature in the spectrum of this object in the 3 μm band.

79 Eurynome

Eurynome is an S-type asteroid. Our AKARI results show a slightly wavy structure with noise, but no significant feature in the 3 μm band.

148 Gallia

Gallia is an S-type asteroid and the largest member of the asteroid family bearing its name (D. Nesvorny 2015[5]). Gallia is a slow rotator, taking 20.66 hr for

one revolution (Warner et al. 2009). Jones et al. (1990) observed Gallia with IRTF and reported no absorption feature in the 3 μm band. Our AKARI results show a wavy structure with noise, but no significant feature in the 3 μm band.

371 Bohemia

Bohemia is an S-type asteroid. The signal observed by AKARI is faint ($\sim$6 mJy in 3 μm, or APmag = 13.89) and the data quality is insufficient to indicate a pattern in the spectral shape at 2.5–3.5 μm, which is almost hidden by noise; thus, no significant features are identified with a sufficient S/N ratio.

532 Herculina

Herculina is an S-type asteroid. Jones et al. (1990) observed Herculina with IRTF and reported no absorption feature in the 3 μm band. Our AKARI results also show no significant feature in the spectrum of this object in the 3 μm band.

8 Flora

Flora is an Sw-type asteroid and has a high spectral slope at 0.45–2.45 μm. Eaton et al. (1983) observed Flora with UKIRT and found a steep slope of the spectrum at 3–4 μm. This spectral shape was considered a continuation of that in shorter wavelengths. Our AKARI data also has a positive spectral slope of $\mathcal{S} = 0.102\,\mu\mathrm{m}^{-1}$, which is higher than the mean value of S-complex asteroids. A small dent shape of uncertain origin with a $\sim$6% band depth appears at around 3.09 μm. Note that only one observation was conducted for this object with AKARI.

89 Julia

Julia is an Sw-type asteroid, the largest member of the asteroid family bearing its name (D. Nesvorny 2015[5]), and considered a parent body of the quasicrystal-bearing CV meteorite Khatyrka (Meier et al. 2018). Our AKARI results show a slightly wavy structure, but no significant feature in the 3 μm band. It has a large positive spectral slope from 2.5 μm to 3.5 μm ($\mathcal{S} = 0.112\,\mu\mathrm{m}^{-1}$).

246 Asporina

Asporina is an A-type asteroid, and is considered a member of the rare olivine-dominated asteroids (e.g., Sanchez et al. 2014). In our AKARI data, a small dent shape with a $\sim$9% band depth appears at around 3.08 μm; however, the AKARI signal is faint ($\sim$11 mJy in 3 μm, or APmag = 13.82) and the data quality is not sufficient for further analysis.

354 Eleonora

Eleonora is an A-type asteroid. There is a possibility that the surface materials of this object contain a pallasite assemblage (Gaffey et al. 2015). In our AKARI data, a small dent shape of uncertain origin with a $\sim$4% band depth appears at around 3.06 μm.

349 Dembowska

Dembowska is an R-type asteroid with a near-infrared spectrum of two strong absorption features at 1 and 2 μm (Bus & Binzel 2002; DeMeo et al. 2009) and has a high albedo of 0.31 (Yu et al. 2017). In our AKARI data, small dent shapes appear at around 2.79 μm (4%) and 3.09 μm (6%), which appear in two pointed observations. A highly negative slope ($\mathcal{S} = -0.033\,\mu\mathrm{m}^{-1}$) of this spectrum is observed at 2.5–4 μm, which might be characteristic of R-type, olivine-rich basaltic asteroids (Leith et al. 2017).

9 Metis

Metis is an L-type asteroid (or S-type in the Tholen taxonomy). Our AKARI results show a bumpy structure at around 2.9 μm, which might be attributable to be contamination by background stars. These are below the detection limit; thus, no obvious features are found in our AKARI data.

387 Aquitania

Aquitania is an L-type asteroid (or S-type in the Tholen taxonomy) and is a slow rotator, taking 24.14 hr for one revolution (Warner et al. 2009). From polarimetric observations (Masiero & Cellino 2009) it is considered a member of the so-called Barbarians (Cellino et al. 2006), which represent some of the oldest surfaces in the solar system. Our AKARI results show a bumpy structure at around 3.1 μm, which might come from contamination due to background stars. These are below the detection limit, and thus no obvious features are found in our AKARI data.

42 Isis

Isis is a K-type asteroid (or S-type in the Tholen taxonomy). An unidentified feature with a $\sim$8% band depth is observed at around 3.09 μm in AKARI data.

4 Discussion

4.1 Advantages and limitations of the AKARI spectroscopic observations

The greatest advantage of the AKARI observations is that they are free from disturbance by telluric absorption and thus able to obtain spectra continuously from 2.5 μm to 5 μm, which can fully cover the peak wavelength of the 2.7 μm band. On the other hand, the effective aperture size of the AKARI telescope is 68.5 cm and the exposure time of each pointed observation is only 10 min in total, which is limited by severe constraints of the attitude control. Thus the present survey provides a flux-limited sample.

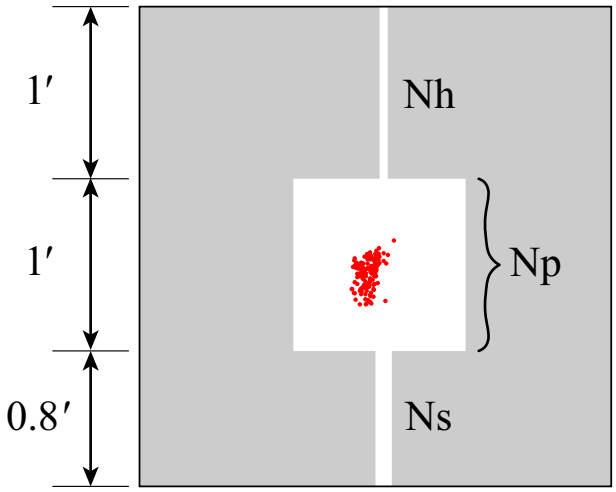

Fig. 20. Distribution of the target positions in the Np window in the reference image (see also figure 3). The gray area is a masked region on the detector. (Color online)

The detection sensitivity is ∼1.3 mJy at 3 μm with 10σ (see the IRC Data User Manual). Note that the sensitivity during Phase 3, the warm mission phase, is likely worse than this because of the temperature change due to degradation of the cryocooler (Onaka et al. 2010). Specifically, the number of hot pixels on the detector increases in Phase 3. To constitute data redundancy, data from two or three pointed observations are averaged to generate reflectance spectra in this study. Spectroscopic observations in the Np window are a type of slitless spectroscopy. The distribution of the target positions in the Np window in the reference image is shown in figure 20. This Np window is effective for observations of point sources, but can be vulnerable to contamination by neighboring stars and ghost images due to nearby bright sources. Our observations were scheduled to avoid the region around the galactic plane, i.e., our targets were located at galactic latitudes of $|b| > 16^{\circ}$. Insufficient flat-fielding is also an issue for the present data set (see subsection 2.2).

4.2 Identification of the 3 μm band shape

In this study, the 3 μm band shape is classified as sharp, w-shape, or 3 μm dent (table 5). This is determined by a combination of $\mathcal{D}_{2.7}$ and $\mathcal{D}_{3.0}$ described in subsection 3.1. This criterion assumes that asteroid spectra contain no narrow or steeply peaking features like atomic or molecular line spectra, but have broad features of typically ∼0.1 μm or wider in the 2.7 or 3.1 μm band.

Classification of the 3 μm band shape is not yet fully established compared to the taxonomies based on the vis-NIR spectra (e.g., Tholen 1984; Bus & Binzel 2002; Lazzaro et al. 2004; DeMeo et al. 2009). Takir and Emery (2012) and Takir, Emery, and McSween (2015a) classified 3 μm band shapes into sharp, rounded, Europa-like, and Ceres-like (hereafter Takir class), while Rivkin et al. (2012) classified them into Pallas-type, Ceres-type, Themis-type, and Lutetia-type (hereafter Rivkin class). These classifications are summarized in table 6. Our classification is generally consistent with Takir class and Rivkin class. Observations with the space telescope in this study detected the 2.7 μm band feature without atmospheric disturbance, which is a big help to classify asteroids into groups of the 3 μm band spectral shape.

Table 6. Candidate of groupings for objects in the 3 μm band shape.

This work	Takir class*	Rivkin class†	Prototypes
Sharp	Sharp	Pallas	2(B), 51(Cgh), 511(C)
W-shape	Ceres	Ceres	1(C), 10(C)
3 μm dent	Rounded	Themis	52(C), 65(Xk)
	Europa		

*Takir and Emery (2012).
†Rivkin et al. (2012).

There are five asteroids among our targets that are classified into the sharp group of the Takir class: 13 Egeria (Ch), 121 Hermione (Ch), 308 Polyxo (T), 511 Davida (C), and 704 Interamnia (Cb). Takir and Emery (2012) reported that this spectral shape is most consistent with the presence of hydrated silicates. Certainly, our AKARI results for these objects show significant absorption features at 2.7 μm. It should be noted that small features appear at around 3.1 μm, which might be obscured by the strong features at 2.7 μm. There are also four asteroids among our targets that are classified into the rounded-shape of the Takir class: 24 Themis (C), 65 Cybele (Xk), 153 Hilda (X), and 361 Bononia (D). Based on AKARI data, 24 Themis has a wider absorption feature at both 2.7 μm and 3.1 μm and is thus classified as w-shape in this study. 153 Hilda and 361 Bononia were not observed with a sufficient S/N with AKARI. Ceres-like objects include 1 Ceres (C) itself and 10 Hygiea (C). These objects display two clear features at 2.7 μm and 3.1 μm with comparable band depths, which belong to the w-shape. Europa-like objects include 52 Europa (C) itself and 451 Patientia (C). Europa seems to have two features at 2.7 μm and 3.1 μm, but the former is too weak to be classified as w-shape. Patientia also has a low S/N spectrum in our data.

In general, it is difficult to classify an object into the featureless category accurately. To make reliable classification, it is necessary to ensure that no features exist within a certain level of accuracy, which requires high S/N data throughout the wavelength of interest. The reflectance spectra obtained in this study include remnant wavy structures on a level of a few percent; thus, it is difficult to

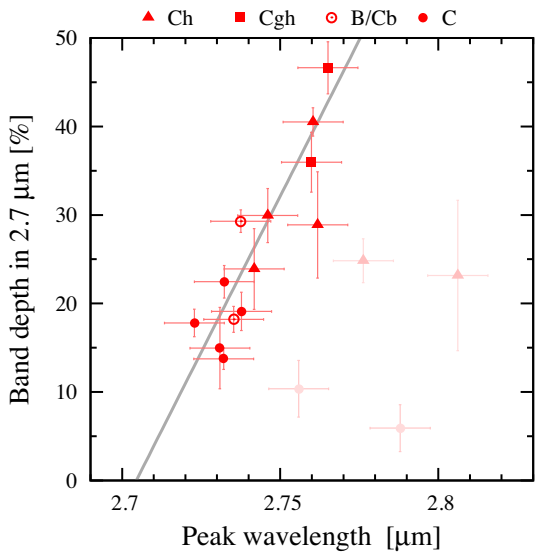

Fig. 21. Relationship between the band depths at 2.7 μm against the peak wavelength for C-complex asteroids. Marks are the same as in figure 1. The correlation coefficient is 0.88. The solid gray line indicates the fitted linear line. The thin red dots denote the asteroid treated as outliers for fitting (see text). (Color online)

distinguish real features from these structures. There are three candidates for featureless spectra in the AKARI data, which have a band depth of less than 2% at 3 μm: 6 Hebe (S-type), 140 Siwa (Xc-type), and 532 Herculina (S-type). Note that 140 Siwa is classified as featureless according to the Takir class (Takir & Emery 2012), which does not show any feature above their noise level in the 3 μm band. 21 Lutetia is reported to have a broad absorption feature in the 3 μm band in the Rivkin class, unlike Pallas, Ceres, or Themis (Rivkin et al. 2011). Our AKARI data, on the other hand, is truncated at $\lambda_{\rm trunc} = 3.57\,\mu$m, and thus the broad spectral shape cannot be fully covered. Featureless spectra can constrain the abundance of surface materials, especially once they are combined with other spectral data. For example, Emery and Brown (2003) reported featureless spectra of 20 Trojan asteroids in the 3 μm region observed with IRTF and these featureless are attributed to the presence of anhydrous silicates (Emery & Brown 2004).

4.3 Peak wavelength in the 2.7 μm band feature

As seen in figure 13, the peak wavelength of the 2.7 μm band feature is concentrated at around 2.75 μm. In particular, C-complex asteroids have a trend between the peak wavelength and the band depth with $S/N > 2$. Figure 21 shows this trend for 17 C-complex asteroids. There are four outliers with longer peak wavelengths: 24 Themis at 2.76 μm, 121 Hermione at 2.81 μm, 127 Johanna at 2.85 μm, and 423 Diotima at 2.79 μm. Except for these four, there is a correlation between the peak wavelength and the band depth among 13 C-complex asteroids:

$$\mathcal{D}_{2.7} = 705.7(\lambda_{\rm peak} - 2.704), \tag{20}$$

where $\mathcal{D}_{2.7}$ is in units of percent (%) and $\lambda_{\rm peak}$ is the peak wavelength in units of μm. The correlation coefficient is 0.88.

The correlation should be used with caution because only 13 asteroids comprise this trend; thus, it may be affected by observational bias. Nevertheless, this correlation may be important for considering asteroid spectra in meteorite research. Based on heating experiments of meteorites in the laboratory, S. Yamashita et al. (in preparation) report a peak-wavelength shift in the 2.7 μm band of hydrated minerals because of the dehydration process. The band depth of the 2.7 μm band indicates an abundance of phyllosilicate, and the peak wavelength of the 2.7 μm band indicates the Mg/Fe ratio in phyllosilicate. During the dehydration process by heating, phyllosilicate decreases and the Mg/Fe ratio simultaneously increase because of the progressive replacement of the phyllosilicates' inter-layer cations Fe^{2+} by Mg^{2+} (e.g., Rubin et al. 2007; Beck et al. 2010; Nakamura et al. 2017). This leads to a decrease of the band depth along with a peak wavelength shift toward shorter wavelengths. Therefore, equation (20) can be interpreted in terms of the meteorite dehydration history.

Some reports detected hydrated minerals on the lunar surface using in-situ observations from spacecrafts: Cassini (Clark 2009), Deep Impact (Sunshine et al. 2009), and Chandrayaan-1 (Pieters et al. 2009). These observations found peak wavelengths near 2.8–3.0 μm. Similar absorption was also detected in the lunar soil of Apollo 16 and 17 (Ichimura et al. 2012). It is considered that the mechanisms forming these lunar hydrated minerals are different from those on asteroids: they may be associated with interaction of the lunar regolith with solar wind proton implantation. These minerals appear to have absorption features near 2.8–3.0 μm. On the other hand, phyllosilicate absorption caused by aqueous alteration in meteorites appears in the vicinity of 2.7 μm (e.g., Rivkin et al. 2015a). Features found in most asteroids observed with AKARI are likely associated with this aqueous alteration.

4.4 Spectral slope in the 3 μm band

The spectral slope measured in the available wavelength range is shown in figure 19. The mean value of the spectral slope of the total 64 objects is $0.047 \pm 0.047\,\mu{\rm m}^{-1}$, which is almost flat at these wavelengths, indicating that the thermal component subtraction described in sub-subsection 2.2.3 works well; if the subtraction was insufficient, it may have caused a significant slope toward longer wavelengths.

The mean value of the slope of each complex is: $\overline{\mathcal{S}(\mathrm{C})} = 0.000 \pm 0.031\,\mu\mathrm{m}^{-1}$, $\overline{\mathcal{S}(\mathrm{X})} = 0.063 \pm 0.041\,\mu\mathrm{m}^{-1}$, and $\overline{\mathcal{S}(\mathrm{S})} = 0.059 \pm 0.045\,\mu\mathrm{m}^{-1}$. The spectral slope makes a major contribution to the derivation of a taxonomic classification of asteroids base on the vis-NIR spectral data (e.g., DeMeo et al. 2009). Our results in this study do not conflict with the trend at shorter wavelengths, that is, C-complex asteroids have a general trend of a flat slope, and X- and S-complex asteroids have a trend of a medium to steep slope. For S-type asteroids, it is known that the space weathering causes a significant change in vis-NIR spectra, in which the albedo decreases (the spectrum becomes darker) and the spectral slope increases (redder) (Yamada et al. 1999). To investigate the space weathering of C-complex asteroids, many laboratory experiments have been conducted (for recent studies, e.g., Matsuoka et al 2017; Lantz et al. 2017). However, it is still in debate whether the space weathering makes the spectral slope of asteroids other than S-type bluer or redder, darker or brighter.

4.5 From dry to wet: characteristics of hydrated asteroids

In the field of meteorite study, it is widely agreed that CM, CI, and CR carbonaceous chondrites, which originate in C-complex asteroids, experienced aqueous alteration in their parent bodies (Brearley 2006 and references cited therein). This aqueous alteration occurred from the reaction of anhydrous rock and liquid water with the isotope decay heat (McAdam et al. 2015 and references cited therein). Correspondingly, from the standpoint of astronomical observations, hydration in asteroids has been discussed with a 0.7 μm absorption feature; C-complex asteroids with an absorption feature in the broad 0.7 μm band are categorized as Ch- or Cgh-type (Bus & Binzel 2002), where suffix "h" represents a hydrated subclass (e.g., Burbine & Bell 1993). This 0.7 μm feature is indicative of an Fe^{2+}—Fe^{3+} charge transfer transition in oxidized iron in phyllosilicates formed through aqueous alteration processes (e.g., Vilas & Gaffey 1989). On the other hand, absorption in the 2.7 μm band is attributed to OH-stretch in hydrated minerals and is a more direct indicator of the presence of water.

Figure 22 shows the number of C-complex asteroids observed in the 0.7 and 2.7 μm bands in this study (cf. Rivkin et al. 2002, 2015a). Figure 23 shows the distribution of band depths in the 0.7 and 2.7 μm bands. The 0.7 μm band depth is measured from the visible spectra compiled by Hasegawa et al. (2017). Rivkin et al. (2015b) discussed the correlation presented in the distribution of the 0.7 and 2.7 μm band depths based on the combined set of asteroid and meteorite measurements. No clear trends are found in figure 23, partly due to a lack of adequate samples for the statistical study. Fornasier et al. (2014) pointed out the relationship between presence/absence of the 0.7 and 2.7 μm band features as follows: if the 0.7 μm band is present on the spectrum, it is always accompanied by the 2.7 μm feature. On the other hand, even if the 0.7 μm band is not found, the 2.7 μm band may still be present on the spectrum. In our measurements, the 0.7 μm band depth is generally weaker by a few percent than that of the 2.7 μm band. Our results confirm those of Fornasier et al. (2014); in addition, not a small number of objects are found without both the 0.7 and 2.7 μm band features. Rivkin (2012) reported that 60%–70% of C-complex asteroids are expected to have hydrated minerals. Our results also indicate that 77% of the observed C-complex asteroids have the 2.7 μm feature, although it may suffer from observational bias.

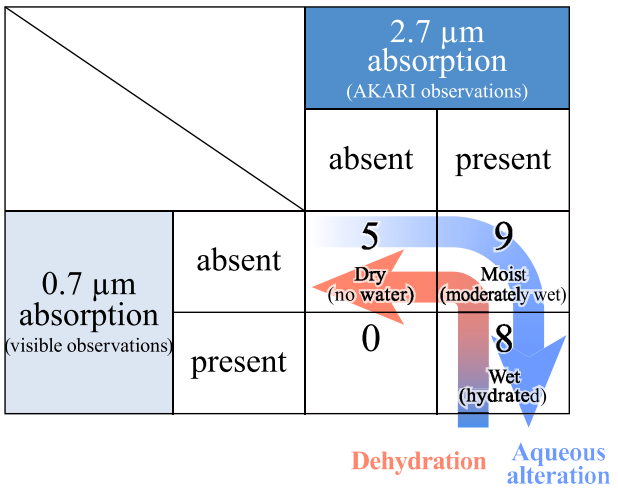

Fig. 22. Matrix of a relation between the 0.7 and 2.7 μm band features in all C-complex asteroids observed in this study. (Color online)

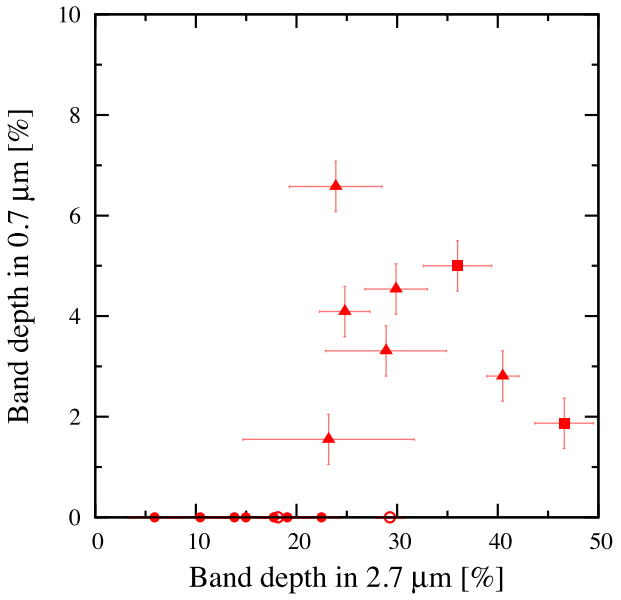

Fig. 23. Correlation between the 2.7 and 0.7 μm band depths in all C-complex asteroids observed in this study. (Color online)

To discuss observational signatures with the aqueous alteration, we classify asteroids into three stages in this study:

- "dry" objects have no feature in either the 0.7 or 2.7 μm bands,
- "moist" objects have a feature only in the 2.7 μm band,
- "wet" objects have features in both the 0.7 and 2.7 μm bands.

It should be stressed that the terms "moist" and "wet" are figurative and not literal in meaning; they do not indicate the presence of water in the form of vapor or liquid, but describe the relative amount of H_2O or OH in minerals. Note that water vapor was detected on 1 Ceres (classified as "moist") with the Herschel Space Observatory (Küppers et al. 2014). Figure 22 can be interpreted in terms of the sequence of aqueous alteration and dehydration process on asteroids with the three stages described above as follows.

(1) An asteroid is "dry" if the signature of aqueous alteration does not appear on its surface—it may be formed in an environment without the presence of water, i.e., dry conditions.
(2) As aqueous alteration progresses to a certain degree, it appears as the 2.7 μm band feature. The object becomes "moist" (or moderately wet).
(3) When aqueous alteration progresses sufficiently, the spectrum shows the 0.7 μm feature and the object becomes "wet". The progress of aqueous alteration does not necessarily progress completely to this stage, and the reaction may stop halfway without the appearance of the 0.7 μm feature.
(4) Dehydration occurs via solar-radiation heat or impact-induced heat. As dehydration progresses, the 0.7 μm feature disappears and the asteroid changes from the "wet" to the "moist" stage.
(5) As dehydration progresses further, the 2.7 μm feature also disappears and the object returns to the "dry" stage.

Let it be added, in this context, that a certain amount of evidence from meteorite study suggests the aqueous alteration of carbonaceous chondrites (e.g., Brearley 2006). These carbonaceous chondrites are considered to originate from C-complex asteroids, or more specifically, formed inside C-complex asteroids (e.g., McSween 1999). In other words, hydrated minerals in C-complex asteroids, which show the 2.7 μm band feature, are considered to be of an internal (endogenic) origin. This suggests that C-complex asteroids were formed in the environment where anhydrous rock and water ice existed together at low temperatures in the protoplanetary disk at the time of planetesimal formation. On the other hand, the degree of aqueous alteration in ordinary chondrites is found to be relatively small (e.g., Brearley 2006). It is consistent with only a few S-complex asteroids showing signatures of aqueous alteration in this study.

The situation of X- and D-complex asteroids is more complicated. The major reason why interpretation of these asteroids is difficult is that there are few spectral counterparts of meteorites found for X- or D-complex asteroids (cf. Kanno et al. 2003; Hiroi & Hasegawa 2003). Nevertheless, it can be considered that low-albedo X-complex (i.e., P-type) and D-complex asteroids may possess properties similar to C-complex ones in the sense of primitive objects (e.g., Vernazza et al. 2015). Thus it is natural that some of these asteroids have signatures of hydration as seen in some stages of C-complex asteroids as the 2.7 μm band feature in this study (e.g., 56 Melete, 476 Hedwig, and 308 Polyxo).

There is an exceptional case found from our results; 349 Dembowska (R-type; olivine-rich, basaltic asteroid, Leith et al. 2017) has a 2.7 μm band feature with 4%. This feature is considered to originate from external (exogenic) materials, which was brought to its surface by hydrated impactors or created by solar wind interactions with silicates. Recent studies also reported that exogenic materials are detected in such traditionally dry asteroids, for example, 4 Vesta (V-type; McCord et al. 2012; De Sanctis et al. 2012), 16 Psyche (M-type; Takir et al. 2017; Avdellidou et al. 2018), and 433 Eros and 1036 Ganymed (S-type; Rivkin et al. 2018). This "contamination" of exogenic materials may be not rare in the main-belt region.

5 Summary

We conducted a near-infrared spectroscopic survey with the AKARI satellite to obtain reflectance spectra of 66 asteroids in the 2.5–5 μm range. These observations successfully fill the gap in the 2.5–2.85 μm data, which cannot be observed with ground-based telescopes. Based on the spectra obtained with AKARI, we found that most C-complex asteroids have clear absorption features related to hydrated minerals at a peak wavelength of approximately 2.75 μm, while no S-complex asteroids have clear absorption in this wavelength.

This data set, comprising direct observations of absorption features in the 2.7 μm band, is quite unique. This study will provide important information on whether asteroid features determined by spacecraft exploration are universal or exceptional. Combining this data set with spectra in shorter wavelengths (<2.5 μm) and comparing it to meteorite spectra measured in the laboratory are both interesting research subjects. These will be discussed at length in future papers. Our spectral data are summarized in the "Asteroid Catalog using AKARI Spectroscopic Observations" (AcuA-spec) and available to the public on the JAXA archive.[7]

[7] ⟨http://www.ir.isas.jaxa.jp/AKARI/Archive/⟩.

Supplementary Data

Supplementary data are available at *PASJ* online.

Supplementary figures S1– S2.

Acknowledgments

This work is based on observations with AKARI, a JAXA project with the participation of ESA. This study was supported by JSPS KAKENHI: Grant Numbers JP15K05277, JP17K05381, and JP17K05636, and partly by the Center of Planetary Science, Kobe University, and the Hypervelocity Impact Facility (former facility name: the Space Plasma Laboratory), ISAS/JAXA. This study utilized the JPL HORIZONS ephemeris generator system, operated at JPL, Pasadena, USA, and Lowell Asteroids Services, operated at Lowell Observatory, Flagstaff, USA. A pilot survey of this work was conducted by Natsuko Okamura and Seiji Sugita (The University of Tokyo). The authors greatly appreciate Takahiro Hiroi (Brown University), Ellen S. Howell (University of Arizona), Zoe A. Landsman (University of Central Florida), Javier Licandro (Instituto de Astrofisica de Canarias), Andrew S. Rivkin (The Johns Hopkins University Applied Physics Laboratory), Driss Takir (SETI Institute), Pierre Vernazza (Laboratoire d'Astrophysique de Marseille), and Makoto Yoshikawa (ISAS/JAXA), for kindly providing their data. FU would like to acknowledge Joshua P. Emery (University of Tennessee), Thomas G. Müller, Victor Alí-Lagoa (Max-Planck-Institut für Extraterrestrische Physik), Daisuke Kuroda (Kyoto University), Tomoki Nakamura (Tohoku University), Takaaki Noguchi (Kyushu University), Sei-ichiro Watanabe (Nagoya University), Takao Nakagawa, Takehiko Wada, Mitsuyoshi Yamagishi (ISAS/JAXA), and Takayuki Ushikubo (Japan Agency for Marine-Earth Science and Technology) for their helpful comments and discussions. Finally, we are very grateful to the anonymous reviewer for careful reading and providing constructive suggestions.

Appendix 1 References of previous studies in the 3 μm band

Reference list of previous spectroscopic observation research in the 3 μm band are given in table 7.

Table 7. Previous works in 3 μm band observations.

Object	Previous works
1 Ceres	Mt.Lemmon (Lebofsky 1978, 1980; Lebofsky et al. 1981), UKIRT (Eaton et al. 1983; Rivkin et al. 2003), IRTF (Jones et al. 1990; Lebofsky et al. 1990; Rivkin et al. 2006b; Rivkin & Volquardsen 2010; Takir et al. 2015b; Vernazza et al. 2005), ISO (Dotto et al. 1999; Rivkin 1997), Stratospheric balloon (Cheng et al. 2017), Dawn (de Sanctis et al. 2015)
2 Pallas	Mt.Lemmon (Larson et al. 1983; Lebofsky 1980), IRTF (Jones et al. 1990) UKIRT (Eaton et al. 1983; Rivkin et al. 2003), ISO (Rivkin 1997)
4 Vesta	Mt.Lemmon (Lebofsky 1980), IRTF (Feierberg et al. 1985; Rivkin et al. 2006a; Vernazza et al. 2005), UKIRT (Hasegawa et al. 2003), Dawn (De Sanctis et al. 2012)
5 Astraea	IRTF (Jones et al. 1990)
6 Hebe	IRTF (Rivkin 1997), UKIRT (Rivkin et al. 2001)
7 Iris	IRTF (Rivkin 1997)
8 Flora	UKIRT (Eaton et al. 1983)
9 Metis	—
10 Hygiea	UKIRT (Eaton et al. 1983), IRTF (Feierberg et al. 1985; Jones et al. 1990; Rivkin et al. 2011; Takir & Emery 2012)
13 Egeria	IRTF (Feierberg et al. 1985; Jones et al. 1990; Rivkin et al. 2015b; Takir et al. 2015a), UKIRT (Rivkin et al. 2003)
16 Psyche	UKIRT (Eaton et al. 1983), IRTF (Jones et al. 1990; Rivkin et al. 1995, 2000; Takir et al. 2017)
21 Lutetia	IRTF (Rivkin et al. 2000; Birlan et al. 2006; Rivkin et al. 2011; Vernazza et al. 2011), Rosetta (Coradini et al. 2011)
22 Kalliope	UKIRT (Eaton et al. 1983), IRTF (Rivkin et al. 2000)
24 Themis	IRTF (Lebofsky et al. 1990; Campins et al. 2010; Rivkin & Emery 2010; Takir & Emery 2012)
33 Polyhymnia	—
40 Harmonia	—
42 Isis	—
44 Nysa	IRTF (Rivkin et al. 1995), UKIRT (Rivkin 1997)

Table 7. (Continued)

Object	Previous works
46 Hestia	—
49 Pales	—
50 Virginia	IRTF (Rivkin et al. 1995)
51 Nemausa	IRTF (Jones et al. 1990; Lebofsky et al. 1990; Rivkin et al. 2015b), UKIRT (Rivkin et al. 2003)
52 Europa	IRTF (Feierberg et al. 1985; Jones et al. 1990; Takir & Emery 2012), UKIRT (Rivkin et al. 2003)
55 Pandora	IRTF (Jones et al. 1990; Rivkin et al. 1995, 2000)
56 Melete	—
64 Angelina	IRTF (Rivkin et al. 1995)
65 Cybele	Mt.Lemmon (Lebofsky 1980), IRTF (Lebofsky et al. 1990; Licandro et al. 2011)
69 Hesperia	IRTF (Landsman et al. 2015)
79 Eurynome	—
81 Terpsichore	—
87 Sylvia	—
89 Julia	—
92 Undina	IRTF (Jones et al. 1990; Rivkin et al. 1995, 2000)
94 Aurora	—
106 Dione	UKIRT (Rivkin et al. 2003)
121 Hermione	IRTF (Hargrove et al. 2012; Takir & Emery 2012)
127 Johanna	IRTF (Rivkin et al. 2015b)
128 Nemesis	—
129 Antigone	IRTF (Rivkin et al. 2000)
135 Hertha	IRTF (Rivkin et al. 2000)
140 Siwa	IRTF (Takir & Emery 2012)
145 Adeona	—
148 Gallia	IRTF (Jones et al. 1990)
153 Hilda	IRTF (Takir & Emery 2012)
161 Athor	IRTF (Rivkin et al. 2000)
173 Ino	IRTF (Jones et al. 1990)
185 Eunike	UKIRT (Rivkin et al. 2003)
216 Kleopatra	IRTF (Rivkin et al. 1995; Landsman et al. 2015)
246 Asporina	—
250 Bettina	—
308 Polyxo	IRTF (Lebofsky et al. 1990; Takir & Emery 2012)
336 Lacadiera	—
349 Dembowska	Mt.Lemmon (Lebofsky 1980)
354 Eleonora	—
361 Bononia	IRTF (Takir & Emery 2012)
371 Bohemia	—
387 Aquitania	—
419 Aurelia	IRTF (Rivkin et al. 2011)
423 Diotima	IRTF (Jones et al. 1990)
451 Patientia	IRTF (Takir & Emery 2012)
476 Hedwig	IRTF (Howell et al. 2011)
511 Davida	IRTF (Feierberg et al. 1985; Jones et al. 1990; Takir & Emery 2012)
532 Herculina	IRTF (Jones et al. 1990)
704 Interamnia	IRTF (Jones et al. 1990; Lebofsky et al. 1990; Takir & Emery 2012), UKIRT (Rivkin et al. 2003)
773 Irmintraud	IRTF (Lebofsky et al. 1990), Subaru (Kanno et al. 2003)
4015 Wilson-Harrington	—

References

Alí-Lagoa, V., et al. 2016, A&A, 591, A14
Alí-Lagoa, V., Müller, T. G., Usui, F., & Hasegawa, S. 2018, A&A, 612, A85
Asensio Ramos, A., & Arregui, I. 2013, A&A, 554, A7
Avdellidou, C., Delbo', M., & Fienga, A. 2018, MNRAS, 475, 3419
Baba, S., et al. 2016, PASJ, 68, 27
Baba, S., et al. 2019, PASJ, 71

Bach, Y. P., Ishiguro, M., & Usui, F. 2017, AJ, 154, 202
Barucci, M. A., & Fulchignoni, M. 2017, A&AR , 25, 3
Beck, P., et al. 2010, Geochim. Cosmochim. Acta, 74, 4881
Beck, P., Quirico, E., Sevestre, D., Montes-Hernandez, G., Pommerol, A., & Schmitt, B. 2011, A&A, 526, A85
Belskaya, I. N., et al. 2005, Icarus, 178, 213
Berk, A., et al. 1999, in SPIE Proc., 3756, Optical Spectroscopic Techniques and Instrumentation for Atmospheric and Space Research III, ed. A. M. Larar (Bellingham: SPIE), 348
Birlan, M., Vernazza, P., Fulchignoni, M., Barucci, M. A., Descamps, P., Binzel, R. P., & Bus, S. J. 2006, A&A, 454, 677
Bowell, E., Hapke, B., Domingue, D., Lumme, K., Peltoniemi, J., & Harris, A. W. 1989, in Asteroids II, ed. R. P. Binzel et al. (Tucson: University of Arizona Press), 524
Brearley, A. J. 2006, in Meteorites and the Early Solar System II, ed. D. S. Lauretta & H. Y. McSween (Tucson: University of Arizona Press), 584
Burbine, T. H. 1998, Meteorit. Planet. Sci., 33, 253
Burbine, T. H., & Bell, J. F. 1993, in 24th Lunar Planet. Sci. Conf., LPI Contrib., 1590, 223
Bus, S. J., & Binzel, R. P. 2002, Icarus, 158, 146
Campins, H., et al. 2010, Nature, 464, 1320
Carruba, V. 2013, MNRAS, 431, 3557
Carry, B., et al. 2010, Icarus, 205, 460
Cellino, A., Belskaya, I. N., Bendjoya, P., Di Martino, M., Gil-Hutton, R., Muinonen, K., & Tedesco, E. F. 2006, Icarus, 180, 565
Cheng, A. F., et al. 2017, Icarus, 281, 404
Clark, R. N. 2009, Science, 326, 562
Clark, R. N., & Roush, T. L. 1984, J. Geophys. Res., 89, 6329
Conrad, A. R., et al. 2007, Icarus, 191, 616
Coradini, A., et al. 2011, Science, 334, 492
Cruikshank, D. P., Geballe, T. R., Owen, T. C., Dalle Ore, C. M., Roush, T. L., Brown, R. H., & Lewis, J. H. 2002, Icarus, 156, 434
Davis, D. R., Farinella, P., & Marzari, F. 1999, Icarus, 137, 140
DeMeo, F. E., Binzel, R. P., Slivan, S. M., & Bus, S. J. 2009, Icarus, 202, 160
De Sanctis, M. C., et al. 2012, ApJ, 758, L36
de Sanctis, M. C., et al. 2015, Nature, 528, 241
De Sanctis, M. C., et al. 2017, Science, 355, 719
Descamps, P., et al. 2008, Icarus, 196, 578
Descamps, P., et al. 2011, Icarus, 211, 2011
Dotto, E., et al. 1999, in ESA-SP 427, The Universe as seen by ISO, ed. P. Cox & M. F. Kessler (Noordwijk: ESA), 165
Dykhuis, M. J., & Greenberg, R. 2015, Icarus, 252, 199
Eaton, N., Green, S. F., McCheyne, R. S., Meadows, A. J., & Veeder, G. J. 1983, Icarus, 55, 245
Egusa, F., Usui, F., Murata, K., Yamashita, T., Yamamura, I., & Onaka, T. 2016, PASJ, 68, 19
Elkins-Tanton, L. T., et al. 2017, in 48th Lunar Planet. Sci. Conf., LPI Contrib., 1964, 1718
Emery, J. P., & Brown, R. H. 2003, Icarus, 164, 104
Emery, J. P., & Brown, R. H. 2004, Icarus, 170, 131
Feierberg, M. A., Lebofsky, L. A., & Tholen, D. J. 1985, Icarus, 63, 183
Fieber-Beyer, S. K., & Gaffey, M. J. 2015, Icarus, 257, 113
Fornasier, S., Lantz, C., Barucci, M. A., & Lazzarin, M. 2014, Icarus, 233, 163
Fornasier, S., Lazzarin, M., Barbieri, C., & Barucci, M. A. 1999, A&AS, 135, 65
Gaffey, M. J., Reddy, V., Fieber-Beyer, S., & Cloutis, E. 2015, Icarus, 250, 623
García-Santos, V., Valor, E., Caselles, V., Ángeles Burgos, M., & Coll, C. 2012, J. Geophys. Res., 117, D19116
Hanuš, J., et al. 2018, Icarus, 299, 84
Hapke, B. 1993, Theory of Reflectance and Emittance Spectroscopy (New York: Cambridge University Press)
Hargrove, K. D., Kelley, M. S., Campins, H., Licandro, J., & Emery, J. 2012, Icarus, 221, 453
Harris, A. W. 1998, Icarus, 131, 291
Hasegawa, S., Kuroda, D., Yanagisawa, K., & Usui, F. 2017, PASJ, 69, 99
Hasegawa, S., Murakawa, K., Ishiguro, M., Nonaka, H., Takato, N., Davis, C. J., Ueno, M., & Hiroi, T. 2003, Geophys. Res. Lett., 30, 2123
Hiroi, T., & Hasegawa, S. 2003, Antartic Meteorite Res., 16, 176
Howell, E. S. 1995, PhD thesis, University of Arizona
Howell, E. S., Rivkin, A. S., Vilas, F., Magri, C., Nolan, M. C., Vervack, R. J., & Fernandez, Y. R. 2011, in Proc. EPSC-DPS Joint Meeting 2011 (Göttingen: Copernicus Publications), 637
Ichimura, A. S., Zent, A. P., Quinn, R. C., Sanchez, M. R., & Taylor, L. A. 2012, Earth Planet. Sci. Lett., 345, 90
Ishiguro, M., et al. 2011, ApJ, 726, 101
Ishihara, D., et al. 2010, A&A, 514, A1
Jones, T. D., Lebofsky, L. A., Lewis, J. S., & Marley, M. S. 1990, Icarus, 88, 172
Kanno, A., et al. 2003, Geophys. Res. Lett., 30, 1909
Kessler, M. F., et al. 1996, A&A, 315, L27
King, T. V. V., Clark, R. N., Calvin, W. M., Sherman, D. M., & Brown, R. H. 1992, Science, 255, 1551
Küppers, M., et al. 2014, Nature, 505, 525
Kuzmanoski, M., & Kovačević, A. 2002, A&A, 395, L17
Landsman, Z. A., Campins, H., Pinilla-Alonso, N., Hanuš, J., & Lorenzi, V. 2015, Icarus, 252, 186
Landsman, Z. A., Emery, J. P., Campins, H., Hanuš, J., Lim, L. F., & Cruikshank, D. P. 2018, Icarus, 304, 58
Lantz, C., Brunetto, R., Barucci, M. A., Fornasier, S., Baklouti, D., Bourçois, J., & Godard, M. 2017, Icarus, 285, 43
Larson, H. P., Feierberg, M. A., & Lebofsky, L. A. 1983, Icarus, 56, 398
Lazzaro, D., Angeli, C. A., Carvano, J. M., Mothé-Diniz, T., Duffard, R., & Florczak, M. 2004, Icarus, 172, 179
Lebofsky, L. A. 1978, MNRAS, 182, 17P
Lebofsky, L. A. 1980, AJ, 85, 573
Lebofsky, L. A., et al. 1986, Icarus, 68, 239
Lebofsky, L. A., Feierberg, M. A., Tokunaga, A. T., Larson, H. P., & Johnson, J. R. 1981, Icarus, 48, 453
Lebofsky, L. A., Jones, T. D., Owensby, P. D., Feierberg, M. A., & Consolmagno, G. J. 1990, Icarus, 83, 16
Lederer, S. M., Domingue, D. L., Thomas-Osip, J. E., Vilas, F., Osip, D. J., Leeds, S. L., & Jarvis, K. S. 2008, Earth Planets Space, 60, 49
Leith, T. B., Moskovitz, N. A., Mayne, R. G., DeMeo, F. E., Takir, D., Burt, B. J., Binzel, R. P., & Pefkou, D. 2017, Icarus, 295, 61
Lemaitre, A., & Morbidelli, A. 1994, Celest. Mech. Dyn. Astron., 60, 29

Licandro, J., Campins, H., Kelley, M., Hargrove, K., Pinilla-Alonso, N., Cruikshank, D., Rivkin, A. S., & Emery, J. 2011, A&A, 525, A34
McAdam, M. M., Sunshine, J. M., Howard, K. T., & McCoy, T. M. 2015, Icarus, 245, 320
McCord, T. B., et al. 2012, Nature, 491, 83
McSween, H. Y., Jr. 1999, Meteorites and Their Parent Planets (New York: Cambridge University Press)
Magri, C., Ostro, S. J., Scheeres, D. J., Nolan, M. C., Giorgini, J. D., Benner, L. A. M., & Margot, J.-L. 2007, Icarus, 186, 152
Mainzer, A., et al. 2011, ApJ, 743, 156
Marchis, F., Descamps, P., Hestroffer, D., & Berthier, J. 2005, Nature, 436, 822
Marchis, F., Kaasalainen, M., Hom, E. F. Y., Berthier, J., Enriquez, J., Hestroffer, D., Le Mignant, D., & de Pater, I. 2006, Icarus, 185, 39
Masiero, J., & Cellino, A. 2009, Icarus, 199, 333
Masiero Joseph, R., Grav, T., Mainzer, A. K., Nugent, C. R., Bauer, J. M., Stevenson, R., & Sonnett, S. 2014, ApJ, 791, 121
Masiero, J. R., Mainzer, A. K., Grav, T., Bauer, J. M., Cutri, R. M., Nugent, C., & Cabrera, M. S. 2012, ApJ, 759, L8
Matsuhara, H., Shibai, H., Onaka, T., & Usui, F. 2005, Adv. Space Res., 36, 1091
Matsuoka, M., et al. 2017, Earth Planets Space, 69, 120
Matter, A., Delbo, M., Carry, B., & Ligori, S. 2013, Icarus, 226, 419
Meier, M. M. M., et al. 2018, Earth Planet. Sci. Lett., 490, 122
Merényi, E., Howell, E. S., Rivkin, A. S., & Lebofsky, L. A. 1997, Icarus, 129, 421
Merline, W. J., et al. 2013, Icarus, 225, 794
Michałowski, T., et al. 2005, A&A, 443, 329
Mogi, K., Yamashita, S., Nakamura, T., Matsuoka, M., Okumura, S., & Furukawa, Y. 2017, in 80th Annual Meeting of the Meteoritical Soc., LPI Contrib., 1987, 6225
Morbidelli, A., & Gladman, B. 1998, Meteorit. Planet. Sci., 33, 999
Mothé-Diniz, T., di Martino, M., Bendjoya, P., Doressoundiram, A., & Migliorini, F. 2001, Icarus, 152, 117
Murakami, H., et al. 2007, PASJ, 59, S369
Nakamura, T., et al. 2017, in 48th Lunar Planet. Sci. Conf., LPI Contribution, 1964, 1954
Ohyama, Y., et al. 2007, PASJ, 59, S411
Onaka, T., et al. 2007, PASJ, 59, S401
Onaka, T., et al. 2010, in SPIE Proc., 7731, Space Telescopes and Instrumentation 2010: Optical, Infrared, and Millimeter Wave, ed. J. M. Oschmann, Jr. et al. (Bellingham: SPIE), 77310M
Onaka, T., et al. 2012, in SPIE Proc., 8442, Space Telescopes and Instrumentation 2012: Optical, Infrared, and Millimeter Wave, ed. M. C. Clampin et al. (Bellingham: SPIE), 844213
Onaka, T., Kaneda, H., Wada, T., Sakon, I., Ita, Y., Takagi, T., & Kim, W. 2008, in SPIE Proc., 7010, Space Telescopes and Instrumentation 2008: Optical, Infrared, and Millimeter, ed. J. M. Oschmann, Jr. et al. (Bellingham: SPIE), 70102X
Ootsubo, T., et al. 2012, ApJ, 752, 15
Ostro, S. J., et al. 2000, Science, 288, 836
Ostro, S. J., Campbell, D. B., & Shapiro, I. I. 1985, Science, 229, 442
Pätzold, M., et al. 2011, Science, 334, 491
Pieters, C. M., et al. 2009, Science, 326, 568
Pilcher, F., Behrend, R., Bernasconi, L., Franco, L., Hills, K., Martin, A., & Ruthroff, J. C. 2014, Minor Planet Bull., 41, 244
Rivkin, A. S. 1997, PhD thesis, University of Arizona
Rivkin, A. S. 2012, Icarus, 221, 744
Rivkin, A. S., Asphaug, E., & Bottke, W. F. 2014, Icarus, 243, 429
Rivkin, A. S., Campins, H., Emery, J. P., Howell, E. S., Licandro, J., Takir, D., & Vilas, F. 2015a, in Asteroids IV, ed. P. Michel et al. (Tucson: University of Arizona Press), 65
Rivkin, A. S., Clark, B. E., Ockert-Bell, M., Volquardsen, E., Howell, E. S., Bus, S. J., Thomas, C. A., & Shepard, M. 2011, Icarus, 216, 62
Rivkin, A. S., Davies, J. K., Clark, B. E., Trilling, D. E., & Brown, R. H. 2001, in 32nd Lunar and Planetary Science Conf., LPI Contrib., 1080, 1723
Rivkin, A. S., Davies, J. K., Johnson, J. R., Ellison, S. L., Trilling, D. E., Brown, R. H., & Lebofsky, L. A. 2003, Meteorit. Planet. Sci., 38, 1383
Rivkin, A. S., & Emery, J. P. 2010, Nature, 464, 1322
Rivkin, A. S., Howell, E. S., Britt, D. T., Lebofsky, L. A., Nolan, M. C., & Branston, D. D. 1995, Icarus, 117, 90
Rivkin, A. S., Howell, E. S., Emery, J. P., & Sunshine, J. 2018, Icarus, 304, 74
Rivkin, A. S., Howell, E. S., Emery, J. P., Volquardsen, E. L., & DeMeo, F. E. 2012, in Euro. Planet. Sci. Congr. 2012, 359
Rivkin, A. S., Howell, E. S., Lebofsky, L. A., Clark, B. E., & Britt, D. T. 2000, Icarus, 145, 351
Rivkin, A. S., Howell, E. S., Vilas, F., & Lebofsky, L. A. 2002, in Asteroids III, ed. W. F. Bottke, Jr. et al. (Tucson: University of Arizona Press), 235
Rivkin, A. S., McFadden, L. A., Binzel, R. P., & Sykes, M. 2006a, Icarus, 180, 464
Rivkin, A. S., Thomas, C. A., Howell, E. S., & Emery, J. P. 2015b, AJ, 150, 198
Rivkin, A. S., & Volquardsen, E. L. 2010, Icarus, 206, 327
Rivkin, A. S., Volquardsen, E. L., & Clark, B. E. 2006b, Icarus, 185, 563
Rubin, A. E., Trigo-Rodríguez, J. M., Huber, H., & Wasson, J. T. 2007, Geochim. Cosmochim. Acta, 71, 2361
Russell, C. T., et al. 2004, Planet. Space Sci., 52, 465
Russell, C. T., & Raymond, C. A. 2011, Space Sci. Rev., 163, 3
Sanchez, J. A., et al. 2014, Icarus, 228, 288
Scaltriti, F., Zappala, V., & Schober, H. J. 1979, Icarus, 37, 133
Schmidt, B. E., et al. 2009, Science, 326, 275
Schmidt, B. E., & Castillo-Rogez, J. C. 2012, Icarus, 218, 478
Shepard, M. K., et al. 2008, Icarus, 195, 184
Shepard, M. K., et al. 2017, Icarus, 281, 388
Shimonishi, T., Onaka, T., Kato, D., Sakon, I., Ita, Y., Kawamura, A., & Kaneda, H. 2013, AJ, 145, 32
Sobrino, J. A., & Cuenca, J. 1999, Appl. Opt., 38, 3931
Sunshine, J. M., Farnham, T. L., Feaga, L. M., Groussin, O., Merlin, F., Milliken, R. E., & A'Hearn, M. F. 2009, Science, 326, 565
Takir, D., & Emery, J. P. 2012, Icarus, 219, 641
Takir, D., Emery, J. P., & McSween, H. Y. 2015a, Icarus, 257, 185
Takir, D., Reddy, V., Sanchez, J. A., Le Corre, L., Hardersen, P. S., & Nathues, A. 2015b, ApJ, 804, L13
Takir, D., Reddy, V., Sanchez, J. A., Shepard, M. K., & Emery, J. P. 2017, AJ, 153, 31
Tholen, D. J. 1984, PhD thesis, University of Arizona
Thomas, C. A., Emery, J. P., Trilling, D. E., Delbó, M., Hora, J. L., & Mueller, M. 2014, Icarus, 228, 217

Usui, F., et al. 2011, PASJ, 63, 1117
Usui, F., Hasegawa, S., Ishiguro, M., Müller, T. G., & Ootsubo, T. 2014, PASJ, 66, 56
Usui, F., Onaka, T., & the AKARI/IRC team, 2018, in JAXA-SP-17-009E, The Cosmic Wheel and the Legacy of the AKARI archive: from galaxies and stars to planets and life, ed. T. Ootsubo et al. (Tokyo: JAXA), 237
Vernazza, P., et al. 2011, Icarus, 216, 650
Vernazza, P., et al. 2015, ApJ, 806, 204
Vernazza, P., Brunetto, R., Binzel, R. P., Perron, C., Fulvio, D., Strazzulla, G., & Fulchignoni, M. 2009, Icarus, 202, 477
Vernazza, P., Mothé-Diniz, T., Barucci, M. A., Birlan, M., Carvano, J. M., Strazzulla, G., Fulchignoni, M., & Migliorini, A. 2005, A&A, 436, 1113
Viikinkoski, M., Hanuš, J., Kaasalainen, M., Marchis, F., & Ďurech, J. 2017, A&A, 607, A117
Vilas, F., & Gaffey, M. J. 1989, Science, 246, 790
Warner, B. D., Harris, A. W., & Pravec, P. 2009, Icarus, 202, 134
Werner, M. W., et al. 2004, ApJS, 154, 1
Yamada, M., et al. 1999, Earth Planets Space, 51, 1265
Yu, L. L., Yang, B., Ji, J., & Ip, W.-H. 2017, MNRAS, 472, 2388
Zellner, B., Tholen, D. J., & Tedesco, E. F. 1985, Icarus, 61, 355